12-2014

Fabrication of a thin silver nanowire composite film and investigation of a patterning technique.

Richard S. Korte 1991-
University of Louisville

Recommended Citation

Korte, Richard S. 1991-, "Fabrication of a thin silver nanowire composite film and investigation of a patterning technique." (2014). *Electronic Theses and Dissertations.* Paper 1997.
https://doi.org/10.18297/etd/1997

FABRICATION OF A THIN SILVER NANOWIRE COMPOSITE FILM AND INVESTIGATION OF A PATTERNING TECHNIQUE

By

Richard S. Korte
B.S., University of Louisville, 2013

A Thesis
Submitted to the Faculty of the
University of Louisville
J. B. Speed School of Engineering
as Partial Fulfillment of the Requirements
for the Professional Degree

MASTER OF ENGINEERING

Department of Chemical Engineering

December 2014

FABRICATION OF A THIN SILVER NANOWIRE COMPOSITE FILM AND INVESTIGATION OF A PATTERNING TECHNIQUE

Submitted by:____________________________________
Richard S. Korte

A Thesis Approved On

____
Date

by the Following Reading and Examination Committee:

____
Gerold A. Willing, Thesis Director

____
Xiao-An Fu

____
Kevin M. Walsh

ACKNOWLEDGEMENTS

I would like to thank Dr. Gerold Willing for giving me the opportunity to work in his research group and for patiently guiding me along the course of my research, Qingwen He for introducing me to her prior work with conductive polymers, Ruvini Dharmadasa for assistance and training on various laboratory equipment, and Dr. Jacek Jacinski and Dr. Tatiana Krentsel for training on materials characterization equipment.

I would like to thank the members of the Reading and Examination Committee, Dr. Gerold Willing, Dr. Xiao-An Fu, and Dr. Kevin Walsh for their willingness to participate and give guidance on my work.

ABSTRACT

Electrically conductive polymers encompass an exciting field of research for applications in dye-sensitized solar cells (DSSC's). DSSC's possess several advantages over other types of solar cells. They offer the potential for high quantum efficiency, solar conversion efficiency approaching that of traditional silicon panels, rapid charge transfer kinetics for photo-excited electrons, mechanical flexibility, and cost efficient manufacturing processes. However, key drawbacks to their large scale production and performance lifetime lie in their reliance on costly indium tin oxide (ITO), fluorinated tin oxide (FTO), and platinum for electrode materials, and the mechanical fragility inherent to a liquid electrolyte layer component.

Much of the current research in the field concerns identifying an effective solid material to replace the liquid electrolyte presently used in DSSC's. Within this field of research, electrically conductive polymers (ECP's) have attracted much interest. One such ECP, PEDOT:PSS [poly(3,4-ethylenedioxythiophene):poly(styrenesulfonate)] has a combination of high flexibility, electrical conductivity, and optical transmittance, making it a viable candidate. Another subset of this research field involves qualifying a cheaper candidate for replacing the costly platinum electrode of DSSC's. Metallic nanoparticles, whose characteristic dimension is on the order of one to hundreds of nanometers, possess unique physical properties emergent at their size scale. Particularly, nanowires of highly conductive metals such as silver deposited on the surface of ECP's raises the possibility of an electrode made using simple bulk processing techniques and using drastically lower quantities of expensive materials for the electrode than typical for DSSC's while offering the same level of conductivity. Furthermore, an interesting challenge lies in patterning the nanowire network using a simple bulk driving force. Achieving facile nanowire alignment, and thus anisotropic electrical conductivity, opens the door to a variety of applications extending beyond solar cell electrodes, such as flexible nanoscale circuitry.

The present thesis describes and evaluates the physical properties of composite thin films of PEDOT:PSS with silver nanowire networks. A simple laboratory scale method for creating a randomly aligned silver nanowire network on PEDOT:PSS is first studied, revealing impressive conductivity increases on the order of 120 versus the bare PEDOT:PSS film. Sheet resistances of the composite films average 37 Ω/□ with average ultraviolet and visible light (UV-Vis) transmittances of 63%. UV-Vis transmittance correlates inversely with the surface concentration of nanowires as expected, with a power regression fit to the data ($R^2 = 0.96$). Of note, no strong correlation is detected between sheet resistance and nanowire surface concentration within the range tested. Additionally, a method for aligning silver nanowires on PEDOT:PSS using a magnetic field is explored. Unfortunately, no significant anisotropy in conductivity is measured using the conditions outlined in these experiments, and explanations are discussed leading into recommendations for future work.

TABLE OF CONTENTS

NOMENCLATURE

A	cross-sectional area of current flow, m^2
$A_{/\!/}$	absorption of light polarized parallel to magnetic field, dimensionless
$A_{\perp}$	absorption of light polarized perpendicular to magnetic field, dimensionless
$A.R.$	nanowire aspect ratio, dimensionless
B	magnetic field strength, T
C	proportionality constant for parallel resistance model, $(s/rad)^{1/2}$
D	nanowire diameter, nm
E	electric potential, V/m
$E.F.$	electrical conductivity enhancement factor, dimensionless
F	sheet resistance correction factor, dimensionless
I	current, A
J	current density, A/m^2
L	sample length along direction of current flow, m
L_n	nanowire length, μm
R	resistance, Ω
R_s	sheet resistance, Ω/□
$R_{s,composite}$	sheet resistance of nanocomposite film, Ω/□
$R_{s,substrate}$	sheet resistance of substrate film, Ω/□
$R_{s,/\!/}$	sheet resistance measured parallel to magnetic field, Ω/□
$R_{s,\perp}$	sheet resistance measured perpendicular to magnetic field, Ω/□
S	nanorod alignment parameter, dimensionless
T	light transmittance, %
t	sample thickness, m
V	voltage, V
W	sample width, m

Greek Symbols

$\alpha_{\parallel}$	longitudinal light polarizability, dimensionless
$\alpha_{\perp}$	transverse light polarizability, dimensionless
λ	wavelength, nm
ρ	resistivity, Ω-m
σ	conductivity, S/m
$\sigma_{composite}$	conductivity of composite film, S/m
$\sigma_{substrate}$	conductivity of substrate film, S/m
$\Delta\chi_v$	anisotropic magnetic susceptibility parameter, dimensionless
ω	rotational speed of spin coating process, rad/s

LIST OF TABLES

LIST OF FIGURES

I. INTRODUCTION

A. Thin Film Sheet Resistance and Electrical Conductivity

Electrical conductivity quantifies the capacity of a material to conduct electrical current. Specifically it relates the amount of current density J, in SI units of amperes per square meter (A/m^2), that will flow through a material with an electrical potential E, in units of volts per meter (V/m) in SI, applied to it. Conductivity, σ, is a temperature-dependent intensive material property, meaning that it is constant for a given material and temperature regardless of its physical form. Having units of Siemens per meter, S/m, it is the reciprocal of resistivity, the tendency of a material to impede the passage of electrical current, which has units of ohm-meters or Ω-m. Current density, electric potential, and resistivity are related by Ohm's law:

$$J = \frac{E}{\rho} \tag{1}$$

When scaled to a specific material size and geometry, Ohm's law can be written in terms of the extensive properties current I (A), voltage V (V), and resistance R (Ω):

$$I = \frac{V}{R} \tag{2}$$

This relation holds well for materials which exhibit a constant proportionality between current and voltage (i.e. a constant resistance) at constant temperature. Such materials are said to be Ohmic. Sheet resistance is a standard used to measure the resistance to the flow of current for thin films of Ohmic material and depends on the material's resistivity and its geometry.

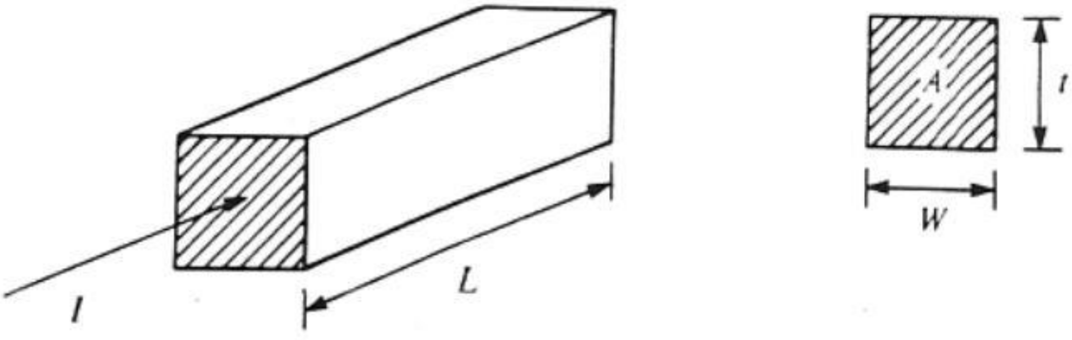

Figure 1. Current Flowing Through a Slab of Material of Rectangular Cross-Section, From [10]

Consider the flow of current through a slab of material as depicted in Figure 1. Current entering the material through the hatched face and exiting from the opposite face not shown will encounter a resistance R proportional to the resistivity of the material, ρ, and the length of the slab L along the direction of conduction but inversely proportional to the cross-sectional area A of the slab. Thus, the extensive quantity resistance is proportional to the length over area with the proportionality constant of resistivity as shown in Equation (3) below. Cross-sectional area can also be expressed as the product of the slab width, W, and thickness, t:

$$R = \rho \frac{L}{A} = \rho \frac{L}{Wt} \tag{3}$$

If the top face of the slab as shown above is taken to have equal length and width, then the ratio L/W becomes unity and the equation reduces to the following form, giving rise to the unique quantity sheet resistance, R_s:

$$R = R_s = \frac{\rho}{t} \tag{4}$$

As such, sheet resistance is the resistance to current flowing in through the rectangular edge of a thin sheet provided that the sheet is square, thus giving it units of not simply ohms but conventionally ohms per square (Ω/□). Uniquely, sheet resistance does not depend on the size of the square, but only its thickness and the material resistivity, assuming uniform current density across the cross section and isotropic resistivity.

The typical device used to measure sheet resistance is the four point probe, depicted conceptually below in Figure 2.

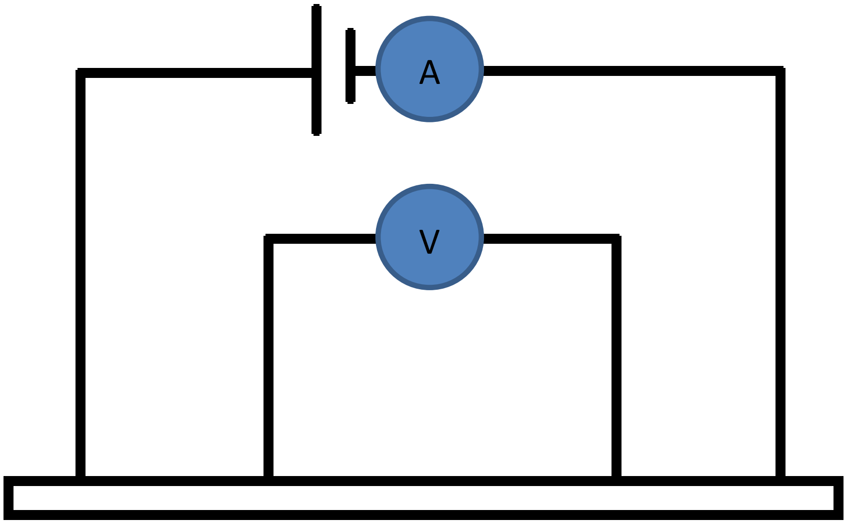

Figure 2. Four Point Probe Diagram

As shown, the device contacts four probes arranged in a line, typically with a constant spacing, to the sample surface. A known current is sent between the outer two probes while the resulting voltage between the inner two probes is measured. Assuming isotropic resistivity of the material, the sheet resistance is related to the measured voltage and applied current in Equation (5) below.

$$R_s = \frac{\rho}{t} = F\frac{V}{I} \tag{5}$$

F is a constant depending on the sample size, probe spacing, and positioning of the probes relative to the sample edge. Experimentally determined values of F which compensate for any effect on the current density distribution that these factors may have are provided in the literature [13]. In the most typical case a geometrically derived relation holds if the probe spacing is much greater than the film thickness and much less than the distance between the measurement point and the sample edge. This arises because essentially a thin, wide sample will have approximately constant current distribution through the film thickness and outward within the plane. Equation (6) below gives this derived relation [20].

$$R_s = \frac{\pi}{\ln 2}\frac{V}{I} \cong 4.53\frac{V}{I} \tag{6}$$

B. Dye-Sensitized Solar Cells

Since its invention in 1988 by Michael Grätzel, the DSSC has been the subject of extensive research efforts spanning over two decades [19]. The vast interest within the research world that DSSC's have sparked stems from the large economic incentive that they would provide over traditional silicon based solar cells. While silicon solar cells depend on high temperature processing of expensive silicon ingots, DSSC's would require far cheaper processing using far less expensive raw materials. Prohibitively high production cost to lifetime ratios currently limit solar cells from competing with fossil fuel systems, making it paramount to find a way to produce solar cells while bypassing the need for expensive materials and processes. However, DSSC's remain unable at large to contend with silicon-based panels in terms of solar conversion efficiency and equipment lifetime.

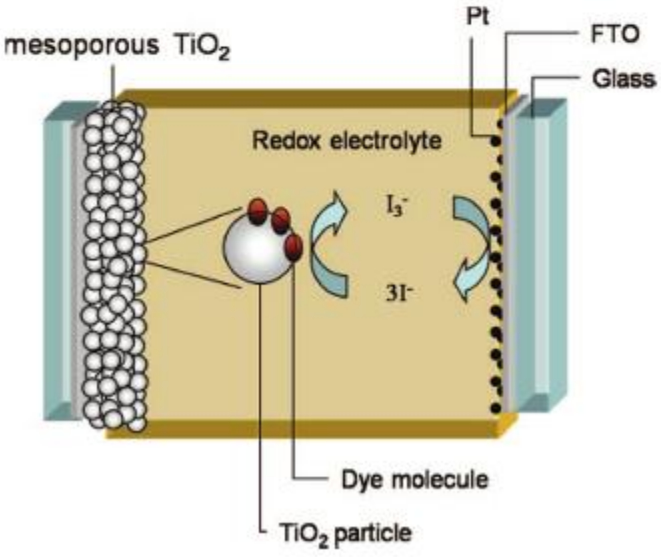

Figure 3. Components and Mechanism of a Dye-Sensitized Solar Cell, From [6]

Figure 3 illustrates the components and mechanisms of a DSSC conceptually. Nanoporous titanium dioxide (TiO_2) coated in a photoactive ruthenium-based dye catalyzes the photon to electricity conversion process. As light shines on the surface of the dye coated TiO_2 layer, the energy of the incoming photons promotes electrons within molecules of the photoactive dye from the stable ground state to a higher energy conduction band state, as shown in Equation (7) below. These excited electrons can flow freely, each leaving behind an oxidized equivalent of the photosensitizer, represented in Equation (8) below. This electrical current flows through the nanostructured TiO_2 to a conductive glass layer where it is channeled away from the DSSC to perform work, then reinjected to the counter electrode composed of platinum on the opposite side of the device from the dye-coated TiO_2 layer. The reinjected electrons enter from the platinum electrode into the charge mediating layer to reduce triiodide anions (I_3^-) to iodide anions (I^-) within a liquid electrolyte solution, shown in Equation (9) below. I^- ions diffuse through the liquid layer toward the dye coated TiO_2 layer where they reduce the oxidized dye molecules back to the neutral ground state, regenerating I_3^- and completing the electrical loop as Equation (10) below shows.

$$hv + S \rightarrow S^* \tag{7}$$

$$S^* \rightarrow S^+ + e^- \tag{8}$$

$$2e^- + I_3^- \rightarrow 3I^- \tag{9}$$

$$3I^- + 2S^+ \rightarrow 2S + I_3^- \tag{10}$$

Electrolyte leakage issues under normal operation have been known to occur. Typically, the electrolyte solution consists of lithium iodide (LiI), sodium iodide (NaI), or a tetraalkylammonium iodide (R_4NI) in an organic solvent such as acetonitrile, propylene carbonate, or propionitrile. The temperature cycling that would inevitably occur in outdoor solar harvesting applications tends to cause an expansion and relaxation cycle for all physical components of the cell, stressing weak points and causing leakage of the liquid electrolyte. Moreover, researchers have discovered through various tests of cell durability that DSSC's suffer from side reactions occurring with the presence of the liquid electrolyte, deteriorating the cell over time [22].

Among many groups motivated to address these concerns, Chung et al. (2012) sought to replace the liquid electrolyte solution of a DSSC with a solid p-type cesium tin iodide ($CsSnI_3$) semiconductor layer. The solid semiconductor layer, able to harvest light at low efficiencies even without a dye-sensitized layer, eliminated the leakage and corrosion problems typical to liquid electrolytes when tested in a full DSSC. Although the group was able to achieve a much higher efficiency of 10.2% than was previously accomplished by other groups using various solid state DSSC alternatives, the fabrication process would still require the use of expensive raw materials and high temperature synthesis of the semiconductor material. Furthermore, creation of the device would require processing toxic polar aprotic solvents such as dimethylformamide. These constraints are counter to the goal of mild, low cost processing techniques.

Another issue hampering the efficiency of DSSCs, although already at a competitive efficiency level of around 10%, is the nature of electron diffusion from the point of photo induced excitation to the electrode at which the current is collected for use. This trap limited diffusion results from the random crystalline networks which exist in the photosensitized nanoparticle films used in DSSC's. Essentially, electrons must make a jump from one nanoparticle to another along the path to the electrode, making for very low diffusivities [25]. Law, et al. (2005) attempted to optimize the mechanism of excitonic electron conduction by using unidirectionally oriented zinc oxide (ZnO) nanowires in lieu of random networks of sintered nanoparticle films. Although they experimentally determined an electron diffusivity through ZnO nanowires two orders of magnitude higher than the best values determined for TiO_2 nanoparticle films, the solar conversion efficiency was merely 1.5%. This stems from a tradeoff introduced by altering the photoelectrode geometry. While oriented nanowire films exhibit higher conductivity of electrons than do nanoparticle films, they possess much less available surface area for harvesting light for initial current generation. Figure 4 below illustrates this in both a conceptual view and a cross-sectional SEM image of an experimental sample.

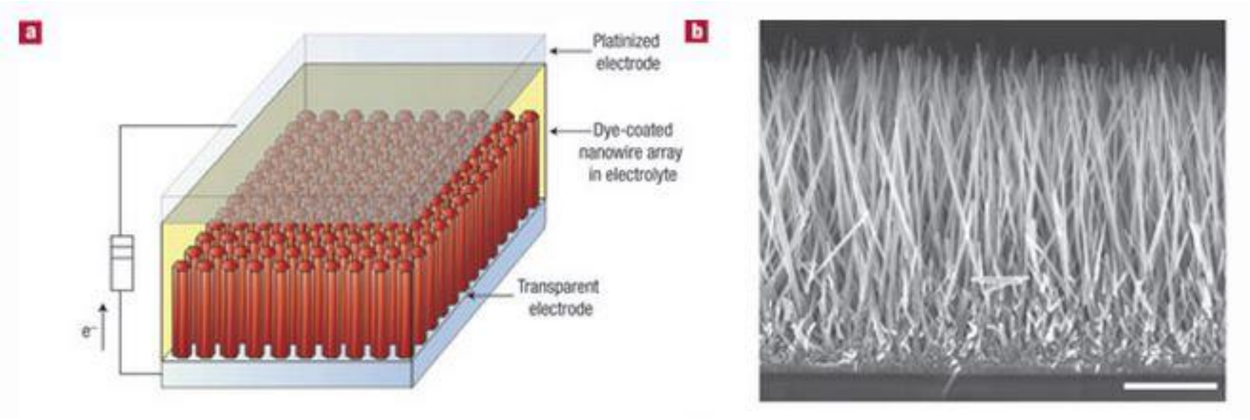

Figure 4. Dye-Sensitized Vertical ZnO Nanowire Arrays, From [16]

Other groups have searched for a material to replace the window electrode for DSSC's. Indium tin oxide (ITO) and fluorinated tin oxide (FTO) have typically been used due to their relatively good conductivity of about 1 S/cm and high optical transmittance of around 80-90%. However, the main issues to be addressed with these conductive glass materials include the limited supply of indium, their low transparency in the near infrared (IR) range of light wavelengths, their susceptibility to corrosion by acids and bases, and their mechanical rigidity. Wang, et al. (2008) produced transparent graphene films with high conductivities around 550 S/cm and excellent thermal and chemical resilience. However, even at thicknesses an order of magnitude lower than the typical for ITO and FTO electrodes, the average optical transmittance only reached about 70%, equating to a significantly lower fraction of light available for harvesting than in DSSC's with ITO or FTO window electrodes. Furthermore, the production of graphene has not yet reached economical large scale production to make this electrode material practical.

C. Silver Nanowire Synthesis Techniques

Within the fields of photovoltaics and optical electronics, silver nanowires have provoked ever increasing interest. Generally, these very high aspect ratio structures with a nanoscale dimension give rise to unique physical, chemical, optical, and electrical properties not observed in bulk macroscopic forms of the same material. Such high aspect ratio nanowires of metals possess intriguing electrical properties because of the confinement of electron motion to distances less than the mean free path of electrons in the bulk metal. Metallic nanowires open the possibility of materials which possess combinations of properties that would not be possible using bulk metals, and can enable drastically lower material usage to achieve a desired level of optical and electrical performance. For instance, metallic nanowires can provide high electrical conductivity and light transmittance due to the lower probability of interaction with photons engendered by their nanoscale width.

The particular focus on silver stems from its having the highest electrical conductivity of any metal, 6.30 X 10^7 S/m. Also influencing research efforts is a slower tendency to rust in the presence of oxygen than copper and its lower cost than gold, two other highly electrically conductive metals which have been used in nanowire syntheses. Thus, a large amount of research effort has devoted itself to creating and refining various techniques for synthesizing silver nanowires.

1. Solution-Based Syntheses of Silver Nanowires

Among the easiest general routes to silver nanowire synthesis outlined in the literature is the liquid solution route. Generally a reagent reduces an ionic silver precursor while a growth directing ligand promotes unidirectional growth of the silver nanoparticles. The difference in lattice spacing between the various facets of monocrystalline silver permits this growth-directing phenomenon. Specifically, the growth directing agent adsorbs onto the (100) plane due to the preferential spacing of atoms along this surface, leaving the (111) plane exposed for attachment of atoms reduced from the ionic precursor.

The work of Murphy, et al. (2001) exemplifies this mechanism in the case of both gold and silver, metals which share highly similar crystalline structures. Murphy's group first reported on an aqueous, room temperature solution processing method for synthesizing nanorods and nanowires of each metal. In their study, reduction of the appropriate metallic salt by sodium borohydride created 4 nm nanoparticle seeds from which nanowires would grow. A small quantity of the silver seed nanoparticles was added to a larger quantity of silver nitrate, ascorbic acid, growth directing agent cetyl trimethylammonium bromide (CTAB), and sodium hydroxide (NaOH) in order to grow the silver nanowires. Intuitively, the ratio of stock silver nitrate and CTAB relative to the silver nanoparticle seed was proportional to the mean aspect ratio of the nanorods produced. A jump to long nanowires occurred when both the ratio was greatly increased and the pH of the solution changed by altering the amount of sodium hydroxide added.

The spacing of atoms in the (100) plane of crystalline silver and gold essentially matches the size of the quaternary ammonium salt head group of CTAB, while that within the (111) plane does not. As illustrated sequentially in Figure 5 below, gold ions supplied will tend to be reduced by sodium borohydride and attach preferentially to the exposed (111) planes of the nanoparticle precursor, while CTAB restricts such growth on the (100) planes. Despite the random motion of silver ions in solution which would otherwise lead probabilistically to spherical nanoparticles, the filtering effect of the CTAB enables high yield synthesis of these silver nanorods and nanowires.

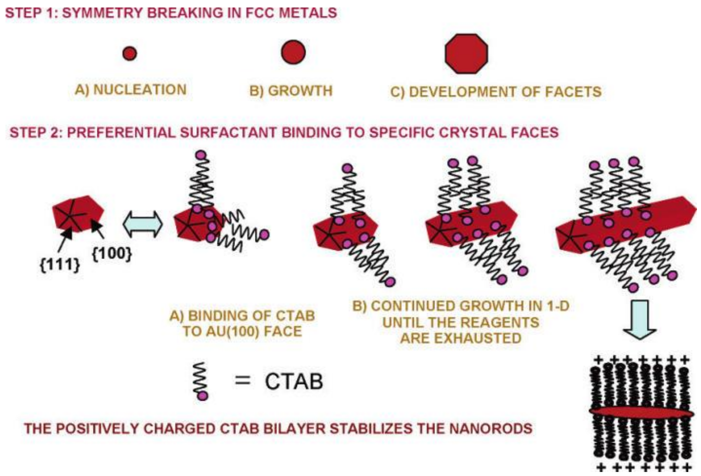

Figure 5. Sequential Axial Growth Mechanism of Gold Nanorods, From [17]

Following shortly from this aqueous, room temperature approach, Sun, et al. (2002) described a method for producing silver nanowires in an ethylene glycol based solution of precursor silver nitrate in the presence of high molecular weight (55,000 g/mol) polyvinylpyrrolidone (PVP) heated to around 170°C, termed the polyol technique. Unlike in the previous aqueous method, ethylene glycol served as both the solvent and the reducing agent for the ionic silver. With a syringe pump, a controlled injection of silver nitrate in ethylene glycol enabled seed nanoparticles of silver to form. In the proposed mechanism, as the crystalline seeds formed the PVP began to coordinate selectively with the (100) crystalline planes of the particles, thereby directing axial growth as further silver nitrate entered the solution.

Wiley, et al (2005) enhanced the synthetic method with the addition of small concentrations of iron (II) to the reaction mixture. The researchers proposed that the iron cations scavenged atomic oxygen developed on the surface of the seed nanoparticles while the chloride anions coordinated with the seed nanoparticles and averted agglomeration by electrostatic repulsion. The image below summarizes this hypothesized mechanism. At higher iron salt concentrations, nearly complete removal of surface oxygen permitted formation of nanowires by preempting oxidative etching of the nanoparticles. Lower iron salt concentrations afforded only partial oxygen removal, allowing for selective oxidative etching and the ultimate formation of nanocubes.

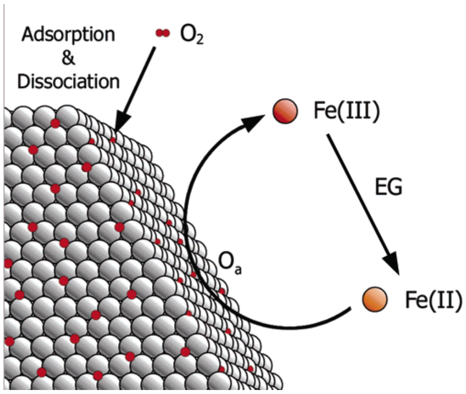

Figure 6. Oxygen Scavenging Effect of Iron (II) Ions, From [30]

Korte, et al. (2008) expanded upon this work with the addition of copper (I) chloride or copper (II) chloride, which essentially functioned in the same manner as the iron salt. However, the use of copper chloride salts did not require a precisely controlled injection of silver nitrate, as was the case for iron chloride salts. The reaction conditions used did not enable reduction of copper (I) to the neutral state by ethylene glycol nor oxidation of neutral silver by copper (I). Thus, the higher availability of copper (I) to scavenge oxygen combined with the unrestricted addition of neutral silver to the nanoparticle seeds allowed facile formation of nanowires. Furthermore, as shown below in Figure 7, a higher chloride concentration was thought to combine to a larger extent with free silver ions and effectively control the rate of silver reduction and addition to the seeds. This equilibrium process forestalled the need for any macroscopically controlled rate of addition of silver by tolerating variation.

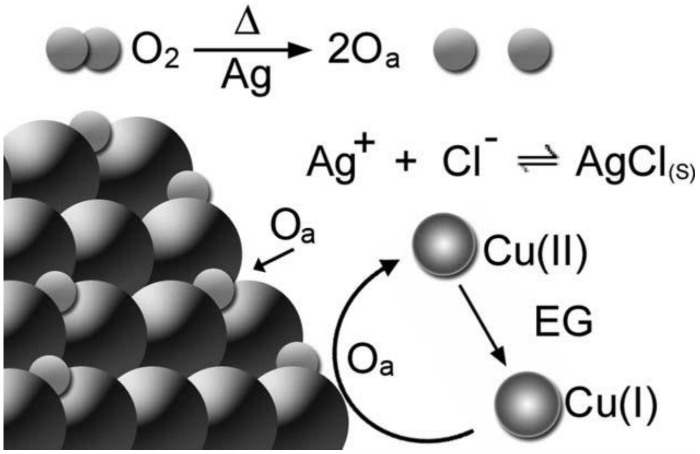

Figure 7. Silver Nanowire Growth Mediating Mechanism of Copper (II) Chloride, From [14]

2. Template-Based Syntheses of Silver Nanowires

Other synthetic routes to grow silver nanowires employ various physical template media. Walter, et al. (2002) grew nanowires of silver and other noble metals using an electrochemical step edge decoration (ESED) technique. Highly ordered graphite sheets served as the substrate upon which the nanowires would grow. A solution composed of silver sulfate, sodium sulfate, and saccharine deposited onto the graphite and subjected to three optimized pulses of electrical potential would selectively grow nanowires at the step edges of graphite. Again, atomic spacing in the crystalline structure of graphite compatible with those of the deposited metals played the key role in directing one-dimensional growth. Figure 8 below gives a basic conceptual diagram of the formation of a metal nanowire on a step edge of graphite.

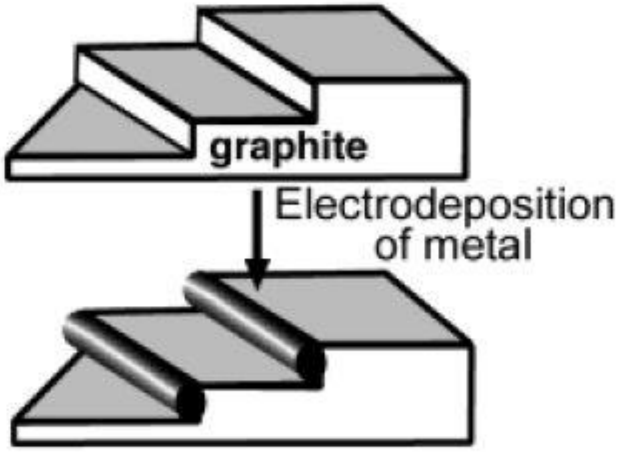

Figure 8. Electrochemical Step Edge Decoration to Create Metal Nanowires, From [27]

Wei, et al. (2005) used uniform nanoporous DNA networks on a mica substrate functionalized with (3-aminopropyl)triethoxysilane (APTES) as the growth medium in their study. Silver ions from a silver nitrate solution were absorbed into the pores of the network and subsequently reduced by immersion into sodium borohydride solution. The process formed either nanoparticles, nanorods, or nanowires by using a low, medium, or high concentration, respectively, of DNA solution initially applied to the APTES-modified mica substrate. Figure 9 below shows an atomic force microscopy (AFM) image of a sample of silver nanowires grown on this DNA template.

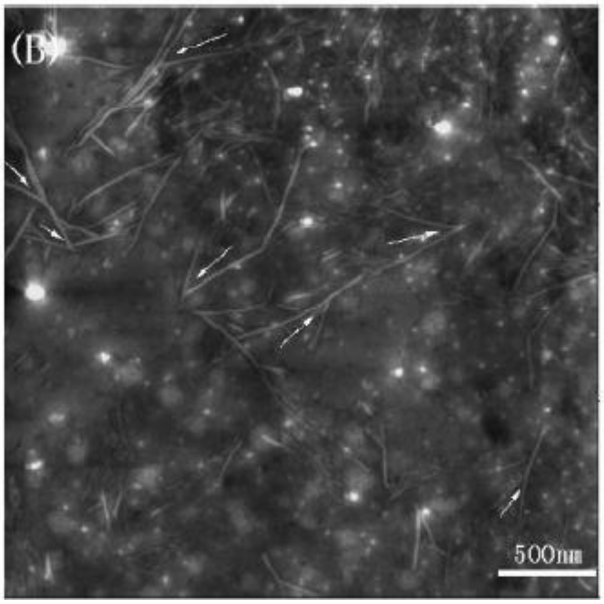

Figure 9. AFM Image of Silver Nanowires on a DNA Network, From [28]

The main disadvantage to this or any other physical template-based approach is reliance on the existing patterning of the starting materials. When considering the potential to scale up the process, the requirement of pre-patterning the starting materials adds another costly processing step. The previously discussed liquid solution techniques circumvent this by exploiting differential growth kinetics corresponding to the various crystalline planes of silver. The natural directing effect does not require costly processing in order to achieve.

D. Silver Nanowire Composite Films for Optical Electronics and Photovoltaics

The facile creation of silver nanowire networks and their deposition onto various substrates has attracted growing interest in the past several years. As discussed previously, silver nanowires can be easily synthesized using liquid solution techniques. Studies have sought to demonstrate their capability to replace expensive electrode materials in solar cells and to function in optical electronics applications. The main appeal of silver nanowire networks lies in their unique combination of high optical transmittance and conductivity, transferability to a variety of substrates, potential for room temperature processing, and mechanical flexibility. Indeed, ITO and FTO glass electrodes in solar cells only possess the first two of this list of characteristics. With this subset of nanocomposite research still growing, efforts have focused first on matching the electrical and optical performance of ITO and FTO. This critical performance benchmarking sets the stage for more complex future work.

Hu, et al. (2010) fabricated a flexible, conductive composite consisting of polyethylene terephthalate (PET) with a randomly oriented network of silver nanowires deposited on the surface using a Meyer rod coating technique. Figure 10 below illustrates this simple technique.

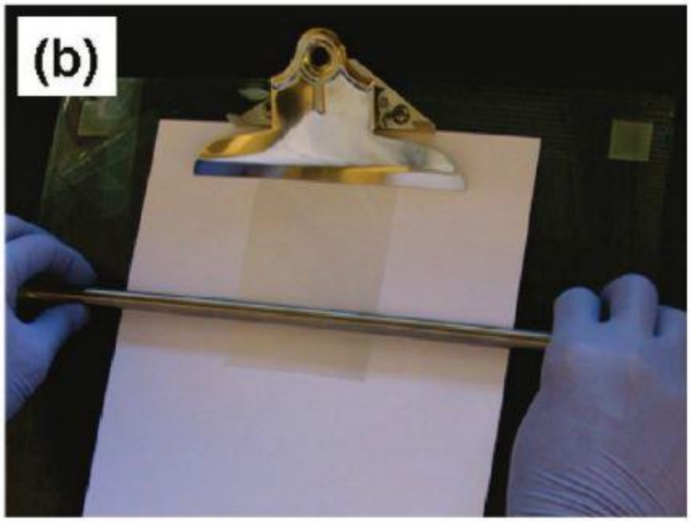

Figure 10. Meyer Rod Coating Technique, From [9]

The group encountered a common tradeoff between low sheet resistance and high optical transmittance. The films with optical transmittance of around 90% in the visible range, comparable to ITO glass, possessed sheet resistances of about 110 Ω/□, while films with sheet resistances as low as about 12 Ω/□ had transmittances of only around 60%. However, a mechanical pressing technique decreased sheet resistances of the films by one order of magnitude on average. Furthermore, by compressing films, the group decreased surface roughness from 110 nm to 47 nm, as displayed in atomic force microscopy (AFM) images in Figure 11 below. The mechanism for further film conductivity enhancement was seen in a scanning electron microscope (SEM) to be the reduction of junction resistance between nanowires. Essentially, the technique both smoothed the surface and bridged gaps between nanowires for enhanced electron flow. The low surface roughness required for organic light emitting diode (OLED) applications makes this composite an interesting choice for further development in OLEDs and solar cell window electrodes. However, the lack of conductivity perpendicular to the plane of the film renders this composite unsuitable for application as a combined hole transport layer and counter electrode layer of a solar cell.

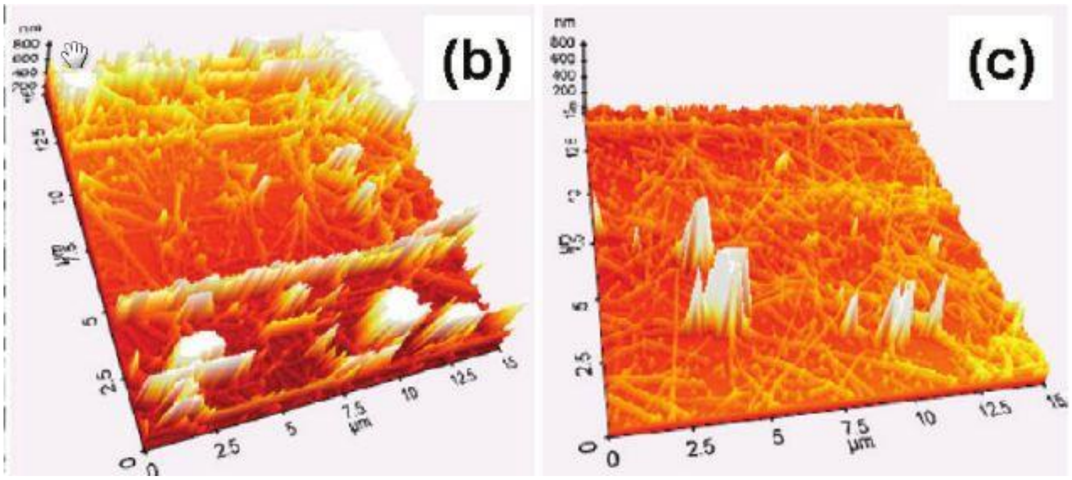

Figure 11. AFM Images of Silver Nanowire Film Before (left) and After (right) Mechanical Pressing, From [9]

Zeng, et al. (2010) created randomly oriented silver nanowire networks buried slightly under the surface of a polyvinyl alcohol (PVA) matrix. Interestingly, by following drop-casting of the nanowire film onto the PET substrate with spin coating of a layer of PVA, the group saw a 10% to 30% reduction in sheet resistance versus the bare silver nanowire networks deposited on PET. The group attributed this slight reduction to a small reduction in junction resistance brought forth by the smoothing action of spin-coating the PVA dispersion onto the nanowire film and thermal drying to create an ultra-thin solid matrix. Whereas Hu, et al. (2010) had achieved low sheet resistances using the shearing action of a simple Meyer rod deposition technique, Zeng, et al. (2010) devised this method to protect the nanowire film from peeling off of the PET substrate due to weak interaction forces between the nanofilm and the polymer substrate. Despite the mechanical and thermal stability of the composite films produced, light transmittance of samples was too low at the nanowire surface concentrations (mg/m^2) necessary to create sheet resistances equal to or less than those of ITO and FTO substrates. Figure 12 below shows their UV-Vis light transmittance spectra for samples of varying sheet resistance.

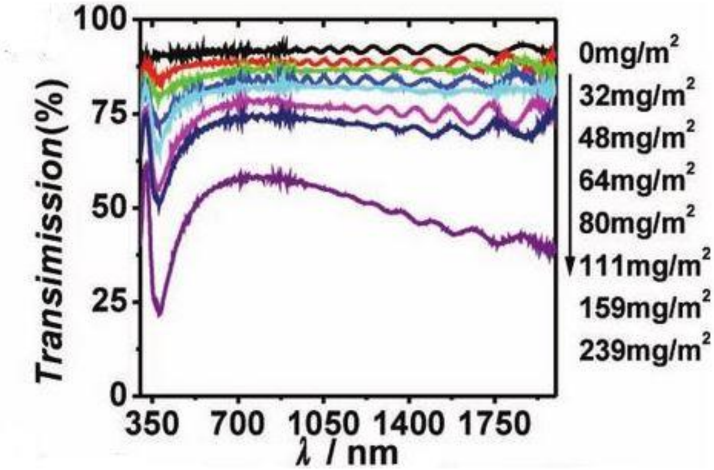

Figure 12. UV-Vis Spectra for PVA-Ag Nanowire-PET Composites, From [32]

Jiu, et al (2012) implemented a different, much more rapid processing method for reducing the silver nanowire junction resistance in randomly oriented networks drop-cast onto PET. The group found that sintering the nanowires with high intensity pulsed light (HIPL) for only 50 µs at light intensities varying from 0.21 J/cm^2 to 1.14 J/cm^2 gave films with sheet resistances four to seven orders of magnitude lower than unsintered samples. The researchers demonstrated through cross-sectional SEM microscopy that the contact between nanowires and their adhesion to the substrate greatly improved due to the brief but extremely intense heating effect of the HIPL sintering. Furthermore, they found damage to the substrate to be negligible because of the brevity of HIPL exposure and its localization to the metallic nanowires. Although not reported, one can infer the nanowire surface concentrations in these experimental efforts to be much lower than those used by Hu, et al. (2010) because of the very high sheet resistance, greater than 1

MΩ/□, measured prior to sintering. However, the huge reduction in sheet resistance to the level of 19 Ω/□ with light transmittances maintained at 82% to 85%, indistinguishable from that of the bare PET film, attests to the superiority of this method for achieving low sheet resistances with low nanowire deposition densities and thus high light transmittances. Figure 13 below shows cross-sectional SEM images of a sample before and after HIPL sintering.

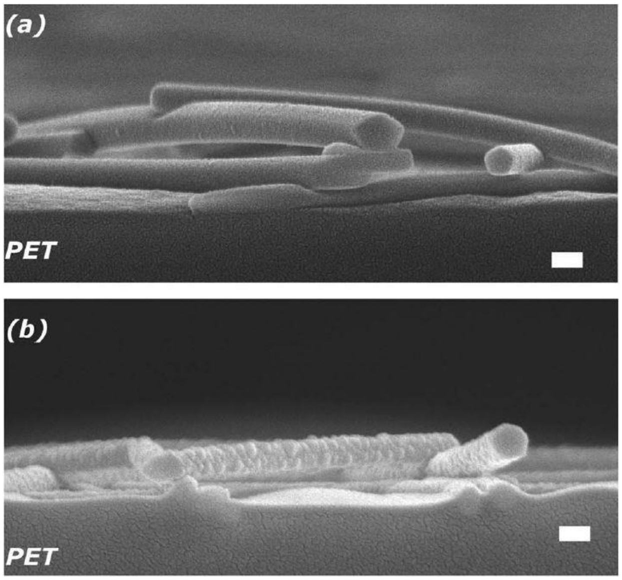

Figure 13. Cross-Sectional SEM Images of Silver Nanowires Before (top) and After (bottom) HIPL Sintering, From [12]

Chen, et al. (2012) fabricated a solar cell with a transparent silver nanowire composite counter electrode layer. The final device contained an ITO window electrode, an ultraviolet and near-infrared sensitive photoactive composite layer, and on top a silver nanowire layer with ITO nanoparticle filler atop a TiO_2 layer for good electrical contact, as depicted schematically in Figure 14 below.

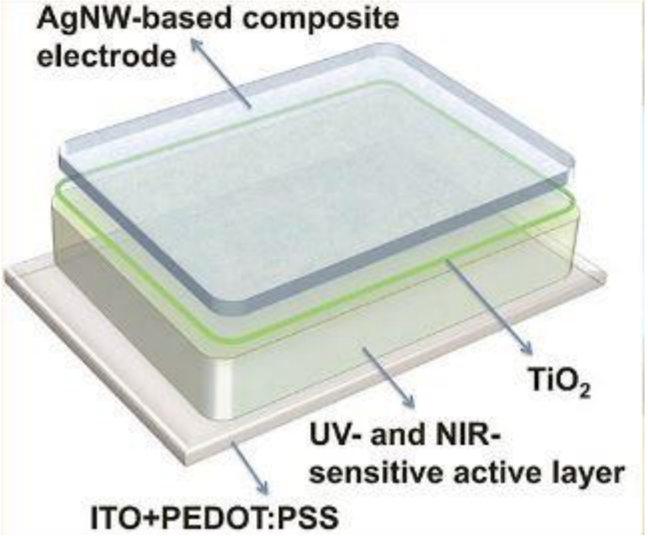

Figure 14. Solar Cell with Transparent Silver Nanowire Composite Counter Electrode, From [3]

The group achieved a good average light transmittance of 80% for the silver nanowire composite layer, as shown below in Figure 15, and good sheet resistance of around 30 Ω/□. However, the light transmittance falls short of an equally thick ITO nanoparticle film. Despite this minor shortcoming, the final device demonstrates with a modest 4% power conversion efficiency that silver nanowires can feasibly be incorporated into organic solar cells.

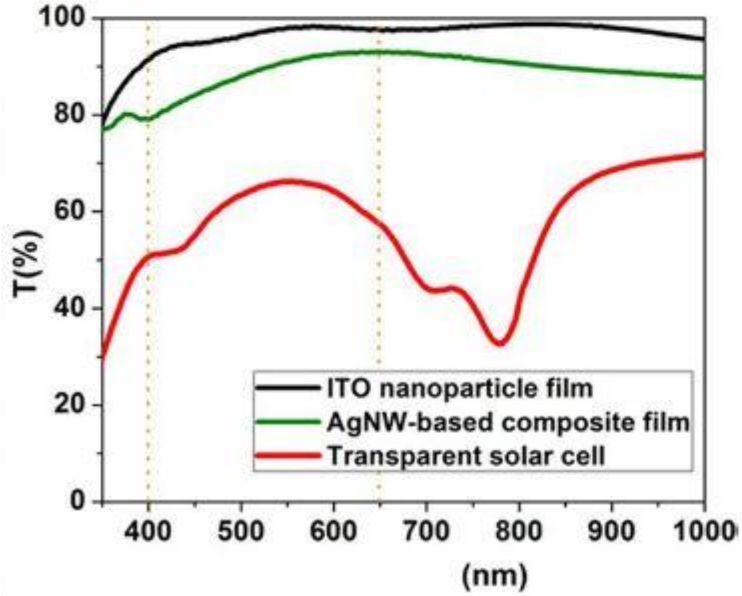

Figure 15. UV-Vis Transmittance Spectra for Silver Nanowire Composite Film, ITO Film, and Final Solar Cell, From [3]

Noh, et al. (2014) invented a one-step spray deposition method for creating PEDOT:PSS thin films with embedded silver nanowires. The films, whose thicknesses were controlled simply by adjusting spray time, exhibited light transmittances and sheet resistances of about 80% and 26 Ω/□, respectively, at one end to 65% and 12 Ω/□ at the other. However, as seen below in Figure 16, the light transmittances are low at the lowest measured wavelengths, and have a peak at around 350 nm, with a broad plateau into the higher wavelengths.

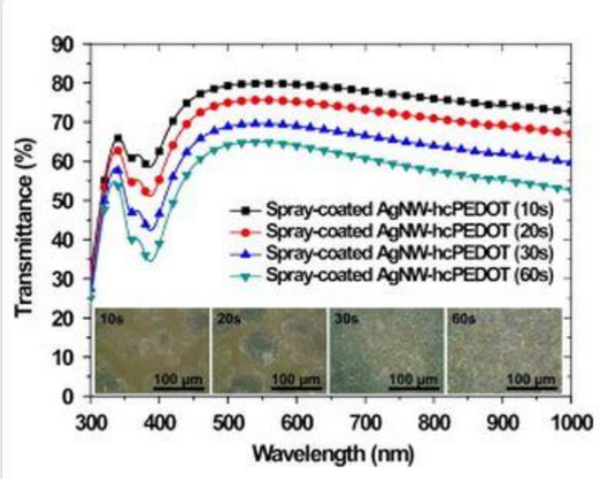

Figure 16. UV-Vis Transmittance Spectra for Various Spray Times, From [18]

This simple technique, which involved spraying an isopropyl alcohol (IPA) based dispersion of silver nanowires and high conductivity grade PEDOT:PSS through a nozzle using nitrogen gas, would render processing time much shorter than for techniques using separate depositions. Figure 17 below shows this processing technique schematically.

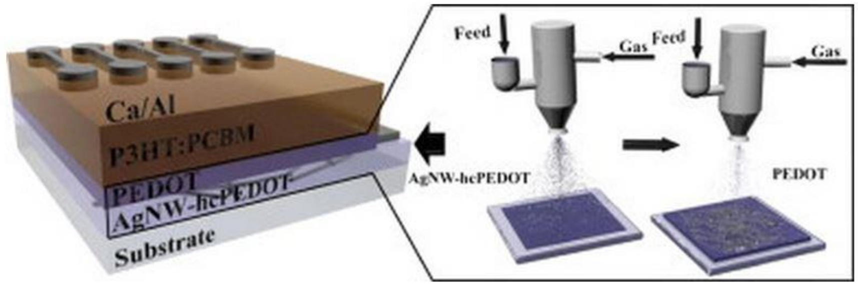

Figure 17. Schematic of Spray Deposition of a Silver Nanowire and PEDOT:PSS Composite Film for a Solar Device, From [18]

Moreover, the process can more feasibly be scaled up to a large scale, streamlined industrial process than can the previously mentioned drop casting, Meyer rod, and spin coating techniques.

E. Nanowire Patterning Techniques

A variety of methods have been demonstrated in the literature for the synthesis and use of silver nanowires in various nanocomposites. Yet none of the aforementioned research groups has reported a bulk processing method for making such conductive nanocomposite films using silver nanowires with a significant degree of unidirectional alignment. Hitherto all efforts have involved randomly oriented silver nanowire films.

Many possibilities, including functional nanoscale circuitry and biological implanted circuits and devices motivate efforts to impose precise patterning on nanowires. Of course, the first hurdle lies in demonstrating basic unidirectional alignment. The present section appraises the various efforts which have achieved this feat with nanowires of various materials. A similar dichotomy to that in nanowire synthesis techniques appears with nanowire alignment techniques: the physical template-based approach and the use of bulk driving forces.

1. Physical Template-Based Approaches to Nanowire Alignment

Xiong, et al (2003) created a synthesis method for crystalline manganese oxide (γ-MnO_2) nanowires using a coordination-organometallic polymer precursor. Directing their work, prior researchers had found that certain organometallic polymers exhibit significant monocrystallinity. Of interest, the regularity of structure and of certain interatomic distances facilitated ordered syntheses of metallic nanowires using liquid solution routes. The group found that the particular crystalline structure of the polymer $[\{Mn(SO4)(4,4'\text{-}bpy)(H_2O)2\}_n]$, shown below in Figure 18, gave way to a preferential unidirectional growth of γ-MnO_2 nanowires when the polymer was oxidized by sodium hydroxide (NaOH) in a mixed solvent of water and methanol.

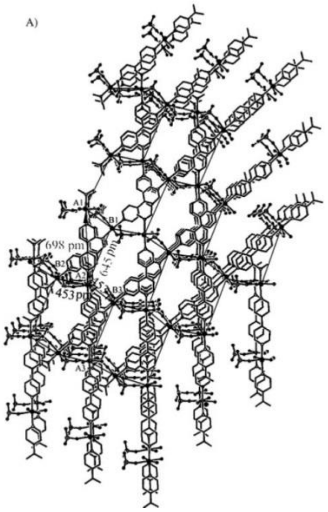

Figure 18. Depiction of the Three-Dimensional Crystalline Structure of [{Mn(SO4)(4,4’-bpy)(H_2O)2}$_n$], From [31]

The regular distribution of distances within the three dimensional polymer structure promoted faster oxidation kinetics along particular spatial directions, translating to the formation of aligned nanowires. Figure 19 below shows an SEM image of their product nanowires.

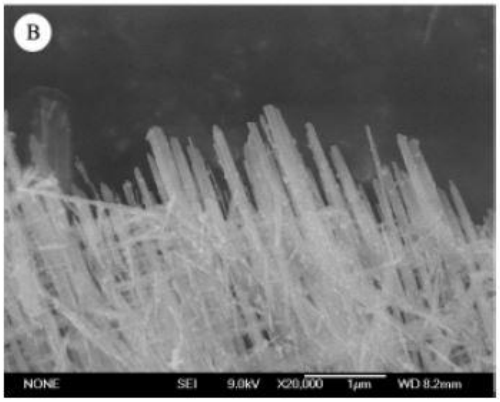

Figure 19. SEM Image of Ordered γ-MnO_2 Nanowires, From [31]

One might envision that similar chemistries can be developed to achieve the same end toward silver nanowires. However, the main limitation barring this general approach from becoming scalable for the manufacture of directionally conductive films is in its reliance on costly low-entropy starting templates. Furthermore, challenges would arise in achieving the planar analog of these three dimensional bundles of metal oxide nanowires.

Correa-Duarte, et al. (2005) electrostatically aligned gold nanorods in an end-to-end fashion along the surface of multiwall carbon nanotubes (MWNT's). Functionalizing the nanorods by exchanging the cationic CTAB surfactant with PVP enabled adhesion to the MWNT's coated with poly(styrene sulfonate) (PSS) followed by cationic poly(diallyldimethyl) ammonium chloride (PDDA). Figure 20 below shows TEM images at different levels of magnification.

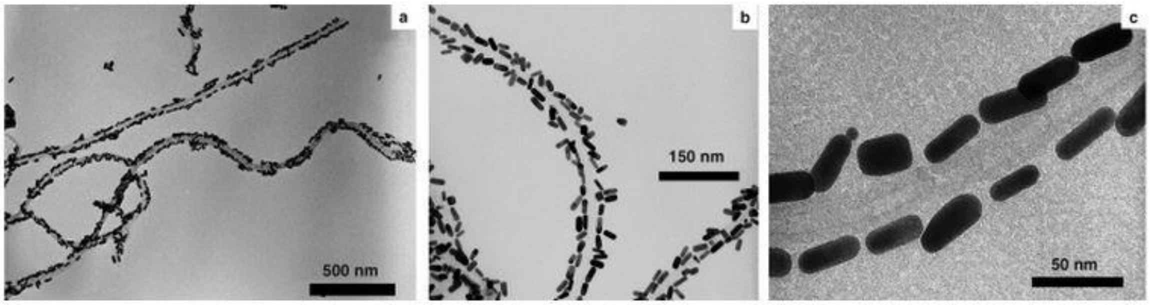

Figure 20. TEM Images of Gold Nanorods Aligned Along Multiwall Carbon Nanotubes, From [5]

2. Bulk Driving Force-Based Approaches to Nanowire Alignment

Cao, et al. (2006) used an electric field to synthesize directly aligned silver nanowires in the absence of any pre-fabricated template. Solid electrolytic $RbAg_4I_5$ films deposited on a NaCl substrate by thermal evaporation served as the growth media for these experiments. Silver films 1 μm thick deposited at the ends of the $RbAg_4I_5$ film served as the electrodes. A constant electric potential applied between the electrodes stimulated the migration of silver ions from the electrolytic film toward the cathode, while the electric current provided the means of electron transfer for reduction of the initial ionic silver within the electrolyte film to the neutral state. The electric potential driving force essentially provided "lines" of least resistance as preferential silver ion migration routes. Thus, as silver combined into nanostructures, the potential favored the formation of silver nanowires as well as alignment of these nanowires with the direction of the electric field. A conceptual schematic of the setup is given below in Figure 21, from their previous work in which they first utilized this setup.

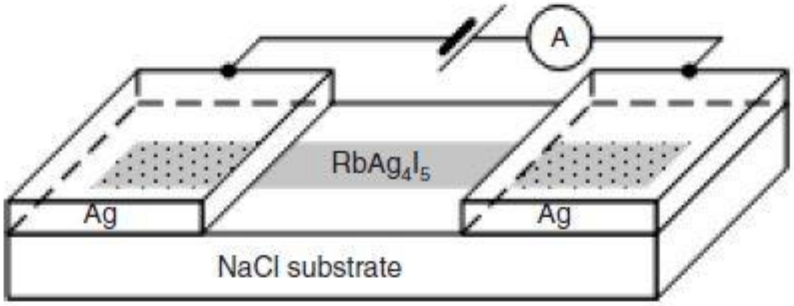

Figure 21. Schematic of Experimental Setup for Synthesis and Alignment of Silver Nanowires Using an Electric Potential, From [2]

Under the application of varying electric potentials, samples exhibited variation in the morphology of the silver nanostructures formed, and in their degree of alignment. Transmission electron microscope (TEM) electron diffraction analysis suggested a single crystalline nature of the nanowires formed. While electric potentials ranging from 100 V/m for 60 minutes up to 400 V/m for only 5 minutes were used, an appreciable degree of alignment and smoothness of the nanowires only emerged under the highest electric potential. Figure 22 below shows an SEM image of the researchers' best results.

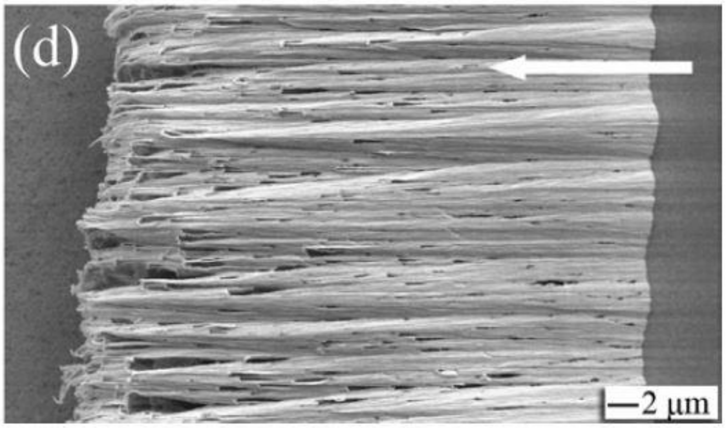

Figure 22. SEM Image of an Aligned Silver Nanowire Bundle (Direction of Electric Field Indicated by Arrow), From [2]

Again, even while the group successfully bypassed the need for a patterned template, their bulk technique still results in an undesirable high degree of agglomeration. Taking into consideration the lack of any pattering of the substrate and silver ion source, $RbAg_4I_5$, the silver ions would tend to migrate with minimal control. Although the group did not postulate in great detail on the exact physical mechanism of silver ion migration, one can speculate on the various forces at play which account for the extensive bundling of these nanowires. The establishment of electric current drives the migration of the positively charged silver ions toward the negatively charged cathode. As this current flow initiates, the exact locations at which silver ions will first reach the cathode remain highly sensitive to a variety of unknown initial conditions. As silver ions do begin to flow, the countercurrent electron flow gives impetus for nearby silver ions to flow along the same channel. One can imagine that because of this, silver nanowire bundles will inevitably form using this technique, placing a limitation on its applicability to films with anisotropic conductivity.

Tao, et al (2003) created aligned silver nanowire monolayers using a Langmuir-Blodgett method. The silver nanowires, prepared using the polyol technique, were functionalized using 1-hexanethiol. These thiol ligands chemisorbed to the surface of the nanowires and displaced the more weakly physisorbed PVP capping agent. Hydrophobic nanowires then formed a random network monolayer above the surface of water within a Langmuir-Blodgett trough, and under large surface pressure underwent a transition from an insulating layer to a conductive layer, while exhibiting a high degree of alignment. Figure 23 below shows photographs of the Langmuir-Blodgett apparatus used. The method also boasts easy transfer onto any arbitrary substrate, suggesting processing flexibility. Figure 24 below shows SEM images of the film at varying magnifications after transfer to a silicon wafer substrate.

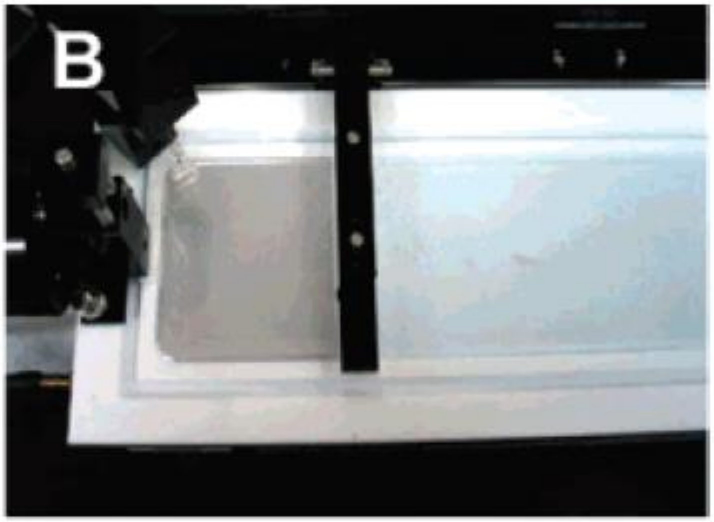

Figure 23. Langmuir-Blodgett Trough with Conductive Silver Nanowire Monolayer, From [24]

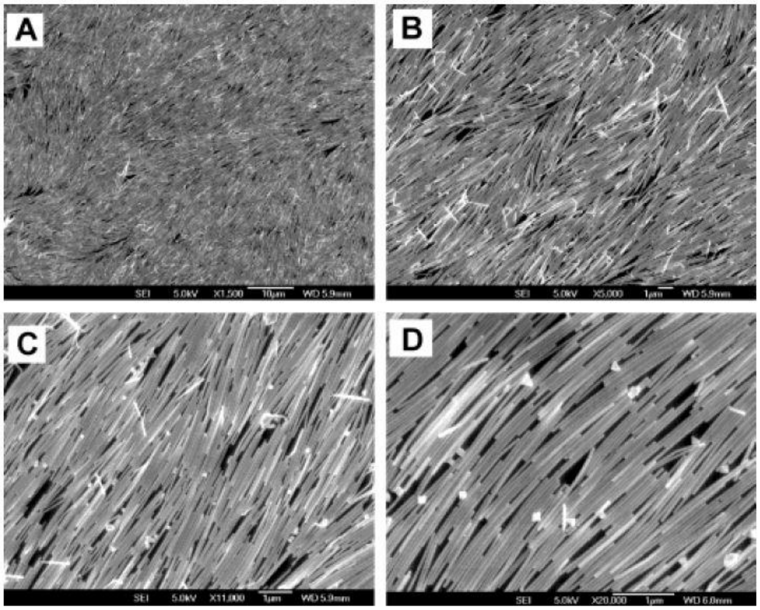

Figure 24. SEM Images of Aligned Silver Nanowire Films on a Silicon Substrate, From [24]

While this method has bypassed the need for any patterned template on which to align nanowires, it suffers from a few drawbacks. The method requires many highly involved processing steps, including the synthesis of the nanowires themselves, functionalization using a thiol ligand, dispersion into a Langmuir-Blodgett trough and compression, and finally transfer to the appropriate substrate. The polyol synthesis route, while it does have a high yield of silver nanowires, requires significant processing time at high temperature and a separation step to isolate nanowires. The hydrophobic functionalization, necessary to promote phase separation and avert agglomeration, requires highly toxic thiols, and multiple separation steps. These would include separation of the hydrophobic phase containing the functionalized silver from the polar ethanol phase and evaporation of the organic solvent prior to the Langmuir-Blodgett step. Finally, careful removal, drying, and transfer of the film from the Langmuir-Blodgett apparatus to the ultimate substrate poses a challenging barrier to large scale production. While easier nanowire synthesis methods do exist, the requisite of hydrophobic functionalization entails the processing of harsh organic solvents.

Shi, et al. (2010) achieved silver nanowire alignment using a three-phase transport route. In their experimental setup, a specific quantity of aqueous silver nanowire suspension deposited onto an immiscible organic phase, chloroform, within a glass container staged the transport and ultimate alignment of nanowires. When added in the proper amount, multiple phase boundaries formed, including the air-water interface, the water-oil interface, and the air-water-oil interface. While SEM characterization, as shown below in Figure 25, showed conclusively that the final result of the nanowire films exhibits a high degree of parallel alignment, the mechanism was left to speculation.

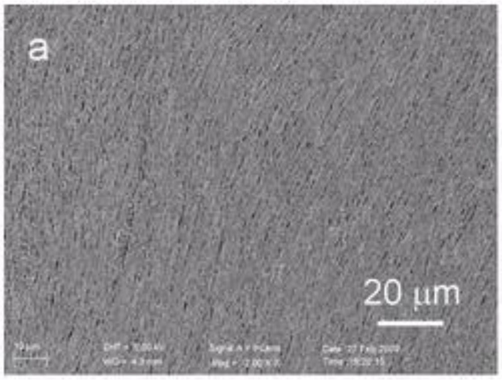

Figure 25. SEM Image of Aligned Silver Nanowire Film Formed by Three Phase Route, From [21]

The group postulated that the evaporation of chloroform resulted in a very slight reduction in pressure of the air-oil interface relative to the pressure of the water-oil interface and thus a negative pressure gradient along the water-oil interface toward the triple phase boundary. It was thought that this pressure gradient mobilized a phase consisting of chloroform (migrating toward the oil-air interface to replenish evaporated chloroform) and silver nanowires. Silver nanowires would then pass through the triple phase boundary and migrate along the water-air interface toward yet another boundary of three phases, the water-air-substrate boundary. Thought to be due to capillary forces, the silver nanowires would spontaneously self-align at this boundary and the film would grow into a continuous layer atop the water phase. Preferential surface interactions between the PVP-coated silver nanowires along their length made this alignment stable. Figure 26 below depicts the mechanism conceptually as well as shows the evolution of the aligned film in macroscopic images.

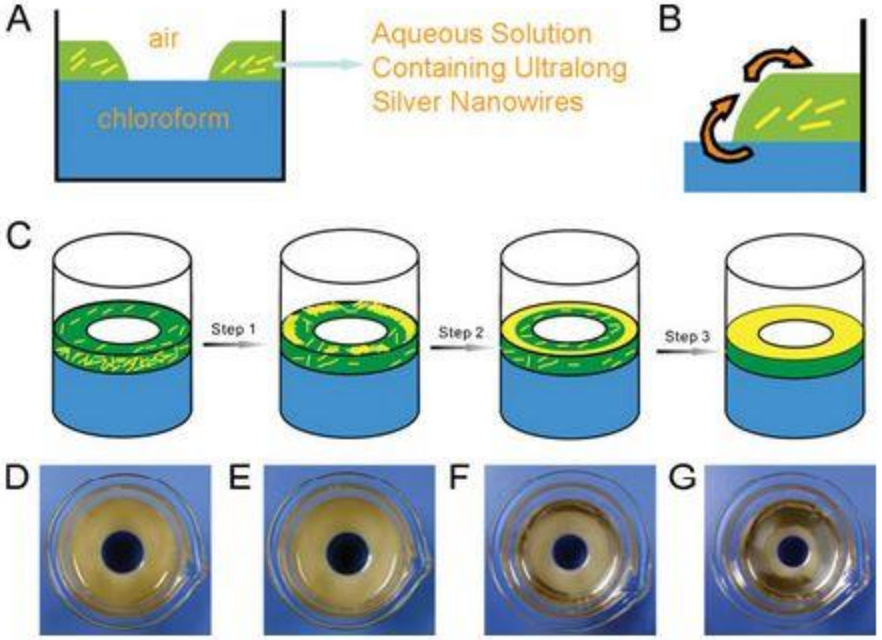

Figure 26. Conceptual Mechanism of Silver Nanowire Transport and Alignment by Three Phase Route and Photographs of Corresponding Steps, From [21]

This method differs from those previously discussed in that it does not require a pre-patterned template or the external application of any force. The carefully controlled ratio of aqueous phase relative to organic phase instead promotes transport by a spontaneously occurring pressure gradient driving force. However, while no external force such as an electric field or a high applied pressure is required, the method relies on a delicate three phase boundary to form and remain undisturbed and on the diffusion kinetics through this boundary. If larger surface area aligned films are to be formed, they would require processing time proportional to their area. These issues constitute limitations on large scale processing.

The use of magnetic fields to induce a high degree of alignment in nanowire arrays has been explored in depth for a variety of nanowire materials. Many efforts have focused on nanowires of metals ferromagnetic in their bulk form. Hangarter, et al. (2005) achieved virtually 100% alignment of nanowires composed of gold or bismuth with ferromagnetic nickel ends on silicon substrates. Nanowires were deposited as wet suspensions on silicon substrates with magnets positioned to induce alignment prior to evaporation of the liquid phase. Again, in 2007, Hangarter's group aligned nanowires of nickel, cobalt, and permalloy ($Ni_{80}Fe_{20}$) radially using a cylindrical coaxial magnet. Similarly, these nanowires were deposited as wet suspensions on glass substrates. Figures 27 and 28 below show SEM images of aligned nanowire structures from these reports. In a similar vein, Lee, et al. (2007) magnetically aligned nickel-capped zinc oxide nanowires deposited as wet suspensions on substrates consisting of silicon with a sputtered and lithographically patterned nickel layer.

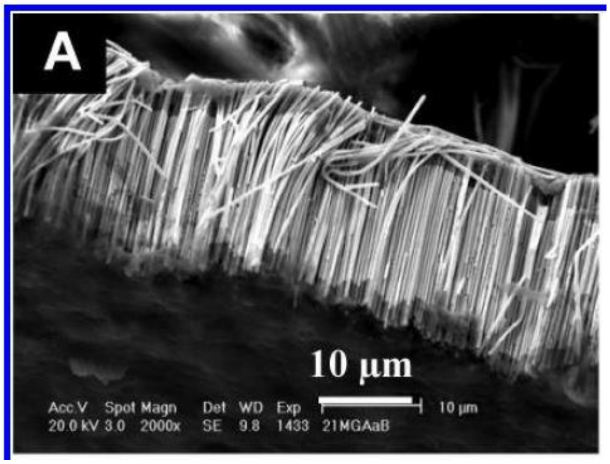

Figure 27. SEM Image of Magnetically Aligned Ni-Au-Ni Segmented Nanowires, From [7]

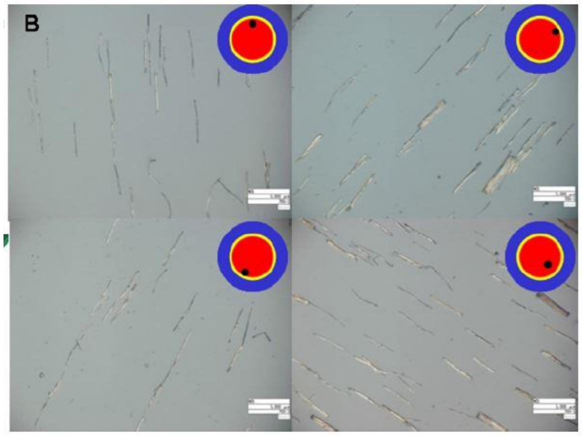

Figure 28. SEM Images of Sample with Nickel Nanowires Radially Aligned by Magnets (Insets show position on sample where corresponding image was taken), From [8]

Nanowires of materials known to be diamagnetic in the bulk form have not attracted the same interest due to the intuition of a dead end. However, at least one report suggests that, as with other property changes observed to differ at the nanoscale from those at the bulk, magnetic properties may also transform at this level. Indeed, van Rhee, et al. (2013) has recently provided evidence of nanorods of gold, a normally diamagnetic material, aligning with a magnetic field. Gold nanorods encapsulated in either CTAB or thiolated polyethylene glycol (mPEG-SH) were aligned in an aqueous suspension subjected to a 33 T magnetic field. Linear dichroism measurements using light polarized both parallel with and perpendicular to the direction of the magnetic field confirmed a significant degree of magnetically induced alignment. From these measurements, a measure of magnetic anisotropy was inferred. The difference in absorption of light of these polarizations was used to calculate the extent of alignment, inferred to be due to anisotropy in magnetic susceptibility:

$$\Delta A(B,\lambda) = A_{\parallel} - A_{\perp} \propto S(B) Im[\alpha_{\parallel}(\lambda) - \alpha_{\perp}(\lambda)] \tag{11}$$

where ΔA is the difference between absorption of light with wavelength λ shone parallel to the magnetic field, B and light shone perpendicular to the magnetic field. S is the magnetic field strength-dependent parameter of interest indicating alignment parallel with or perpendicular to the magnetic field, with positive values showing parallel alignment and negative values showing perpendicular alignment. The α parameters (from left to right) are the longitudinal and transverse light polarizabilities of the gold nanorods for a given wavelength of light. Table I below summarizes results of gold nanorod alignment for a variety of nanorod sizes, aspect ratios, and concentrations.

TABLE I

RESULTS FOR MAGNETIC ALIGNMENT OF GOLD NANORODS, From [26]

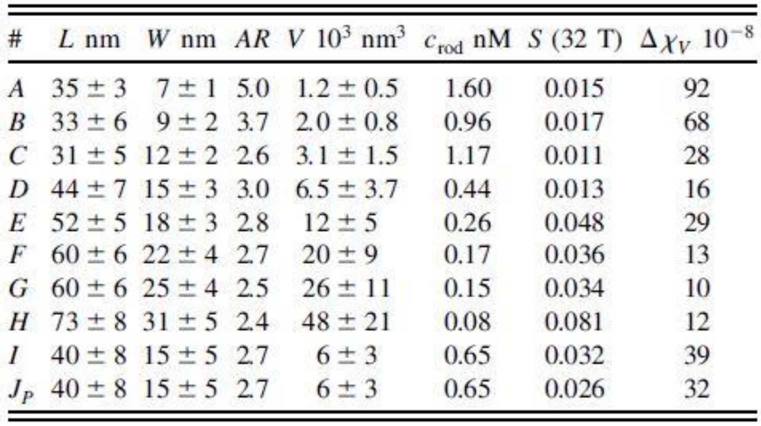

#	L nm	W nm	AR	V 10^3 nm^3	c_{rod} nM	S (32 T)	$\Delta\chi_V$ 10^{-8}
A	35 ± 3	7 ± 1	5.0	1.2 ± 0.5	1.60	0.015	92
B	33 ± 6	9 ± 2	3.7	2.0 ± 0.8	0.96	0.017	68
C	31 ± 5	12 ± 2	2.6	3.1 ± 1.5	1.17	0.011	28
D	44 ± 7	15 ± 3	3.0	6.5 ± 3.7	0.44	0.013	16
E	52 ± 5	18 ± 3	2.8	12 ± 5	0.26	0.048	29
F	60 ± 6	22 ± 4	2.7	20 ± 9	0.17	0.036	13
G	60 ± 6	25 ± 4	2.5	26 ± 11	0.15	0.034	10
H	73 ± 8	31 ± 5	2.4	48 ± 21	0.08	0.081	12
I	40 ± 8	15 ± 5	2.7	6 ± 3	0.65	0.032	39
J_P	40 ± 8	15 ± 5	2.7	6 ± 3	0.65	0.026	32

$\Delta\chi_v$ is the difference between longitudinal and transverse magnetic susceptibilities calculated from the parameter S. Interestingly, while others observing the same effect have speculated that the magnetic anisotropy of gold nanorods was due to electron interactions with ligands, this work suggests that this is not the case due to the nearly unchanged free electron densities on the gold nanorod surfaces. As further evidence supporting this notion, varying the concentration of the ligands at a constant nanorod size showed no difference in alignment extent. However, a dependence on nanorod aspect ratio was observed, as shown below in Figure 29, a plot of $\Delta\chi_v$ vs. aspect ratio, AR.

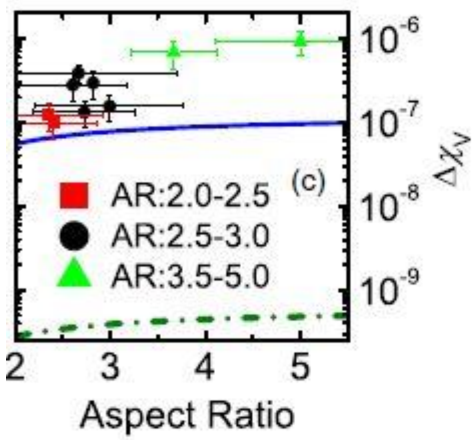

Figure 29. Plot of Anisotropic Magnetic Susceptibility versus Nanorod Aspect Ratio, From [26]

Overall, the previous survey of techniques to spatially manipulate various types of nanowires offers several possibilities from which to expand. However, a few categories exhibit drawbacks as highlighted previously. The nanoscale patterned physical template approaches do not show great promise for bulk processing due to their need for costly pre-processed substrates. The electric field approach suffers poor morphology and inevitable bundling. The three phase transport and Langmuir-Blodgett approaches result in a high degree alignment but with no assurance that it will occur along a known direction. The use of a magnetic field, however, initially shows promise for the facile creation of a unidirectionally conductive composite of PEDOT:PSS and a silver nanowire film, and was the basis for the setup explored in this thesis. Because of the positive correlation between nanorod aspect ratio and anisotropic magnetic susceptibility observed by van Rhee, et al. (2013), the expected continuation of this trend at very high aspect ratios made silver nanowires highly appealing for study. Moreover, the knowledge of the direction of the magnetic field applied would lend a simple prediction of the alignment that would occur at the nanoscale, prior to any advanced characterization.

In this thesis, we define a simple method for creating a silver nanowire composite film on a PEDOT:PSS substrate, with the goal of achieving high optical transmittance paired with high electrical conductivity. Although composites presented in this work do not fit the conventional definition of composites in that they consist of heterogeneous layers, we will treat them as such with regard to bulk electrical conductivity. We also develop and evaluate a method for aligning silver nanowires on PEDOT:PSS using a magnetic field with the aim of anisotropic conductivity. We examine the effect in general of nanowire surface concentration as well as the unforeseen factors and complexities that arose in the course of this research, comparing the results of this work to the present best efforts in the literature.

II. MATERIALS AND METHODS

All materials used in these studies were obtained from Sigma Aldrich and used as provided, without additional treatment. Table II below lists materials used in the experiments and corresponding product numbers. All glassware used was first thoroughly cleaned using standard dish soap and subsequently rinsed with deionized water. Deionized water was used to prepare all aqueous solutions mentioned below, (*Thermo Scientific Barnstead Mega-Pure Water Distillation Apparatus* Asheville, NC, USA).

TABLE II

MATERIALS AND SPECIFICATIONS

Material	**Product Number**
silver nitrate	209139
sodium borohydride	71321
decyltrimethylammonium bromide	30725
dodecyltrimethylammonium bromide	D8638
trisodium citrate dihydrate	S1804
L-ascorbic acid	A7506
sodium hydroxide (anhydrous pellets)	S5881
polyvinylpyrrolidone	PVP360
ethlyene glycol	324558
iron (III) chloride	157740
poly(3,4-ethylenedioxythiophene)-poly(styrenesulfonate) (dry redispersible pellets)	768618

A. Silver Nanowire Synthesis, Separation, and Characterization

During the course of research for the present thesis, two distinct approaches outlined previously were used to synthesize silver nanowires. First, the aqueous solution phase approach previously reported was attempted [11]. The 4 nm silver NP seeds were produced by making a 200 mL solution with a final concentration of 0.25 mM silver nitrate and 0.25 mM sodium citrate. To this solution 6.0 mL of 10 mM aqueous sodium borohydride was added all in one dose under vigorous stirring on a magnetic stir plate.

Within a few seconds the solution became a translucent golden brown. Note that this quantity of solution used was scaled up from that of the original reported procedure by a factor of ten in order to reduce the measurement error associated with weighing extremely minute quantities of solutes.

Figure 30. Silver Nanowire Seed Solution

The stock solution was prepared in another 250 mL Erlenmeyer flask cleaned in the same manner as described above. The composition of this stock solution is given in Table III below.

TABLE III

COMPOSITION OF SOLUTIONS FOR SILVER NANOWIRE SYNTHESIS

Component	**Quantity (mL)**	**Concentration (mM)**
silver nitrate solution	2.5	10
ascorbic acid solution	5.0	100
dodecyltrimethylammonium bromide solution	93.0	80

To this stock solution 2.5 mL of the NP seed solution and 0.5 mL of 1 M sodium hydroxide was added with just enough gentle shaking to homogenize the mixture. Within 15 min the contents of the flask turned a translucent yellow, as shown below in Figure 31.

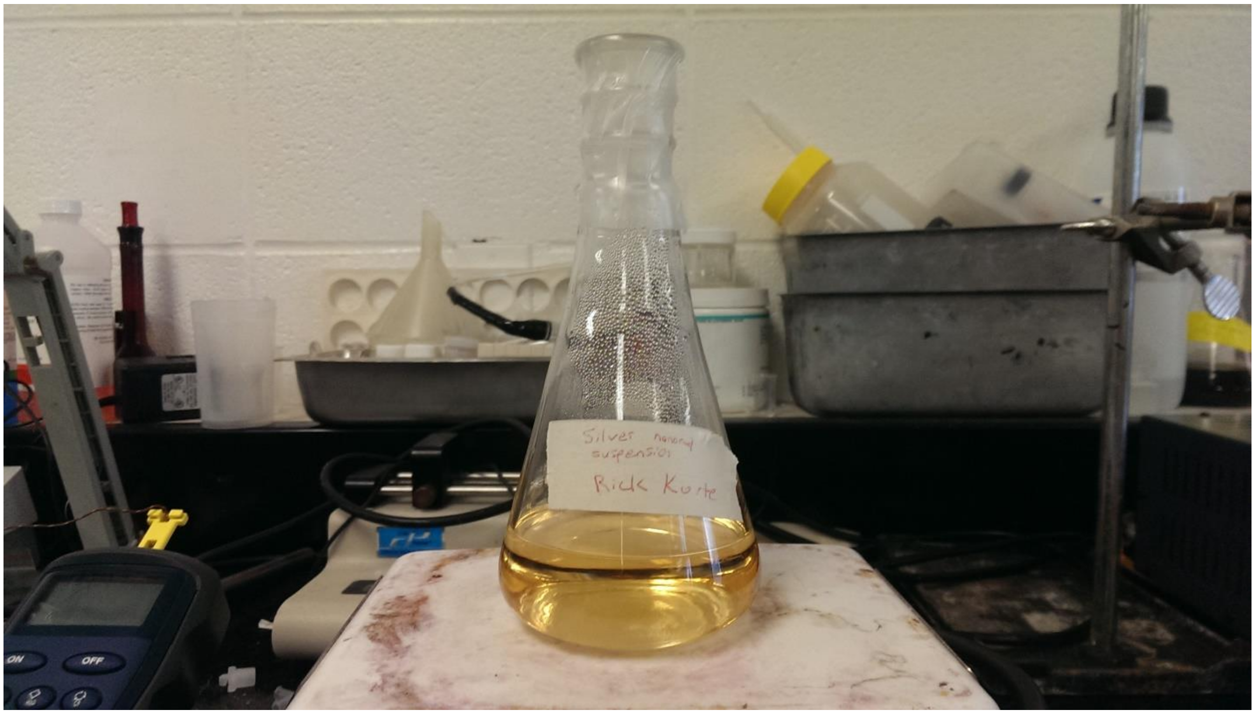

Figure 31. Silver Nanowire Suspension

Although the synthesis appeared successful at a glance considering the conformance of observations to those reported in the literature, a practical limitation loomed. A calculation based on the quantities of silver given above and an assumed 50% conversion of silver to nanowires gives a total of only 2.77 mg of silver nanowires in the final product suspension. Although originally thought to be sufficient for further experimental purposes, the prohibitively small quantity of silver proved impractical to precipitate by centrifugation. Simply scaling up the total size of the reaction mixture would have increased the quantity of silver product. However this scale-up factor would have had to be very large, to the point that homogenizing the mixture upon the addition of sodium hydroxide solution would have introduced variation in the initial reaction kinetics by requiring a much larger characteristic time for complete mixing. Increasing the concentrations of reagents would represent a major deviation from the exact conditions reported in the literature, leading in all likelihood to an unknown quality of silver product. Because of the inability to separate perceptible amounts of silver nanowires from the suspension according to the prescribed synthesis, this method, despite its simplicity, was abandoned in favor of an alternative.

The polyol synthesis technique described above was then chosen because, although it required heating to above 150 °C for 1.5 hours, it had the capability to generate a meaningful amount of silver nanowire product. First, a 0.6 mM iron (III) chloride ($FeCl_3$) solution in ethylene glycol (EG) was prepared by weighing out between 15 and 25 mg of the solute and mixing it into the appropriate amount of ethylene glycol. A dispersion of polyvinylpyrrolidone (PVP, number average molecular weight of 360,000 g/mol) in ethylene glycol was then prepared. This step proved very tedious in order to fully disperse the high molecular weight polymer without excessive clumping, and required repeated adjustment. A total of 294 mg of PVP was added a few granules at a time to a 50 mL flask containing 33.69 mL of EG heated to around 80 °C with vigorous stirring on a magnetic stir/heating plate. When added too quickly on initial attempts, the PVP clumped irreversibly within the vortex and would eventually settle to the bottom and overheat, melting it into a coherent, non-dispersible mass. The PVP dispersion was then heated to 150 °C under stirring for 1.5 hours, with fiberglass insulation wrapped around the sides of the flask to promote efficient heating and minimal temperature gradients, as depicted below in Figure 32.

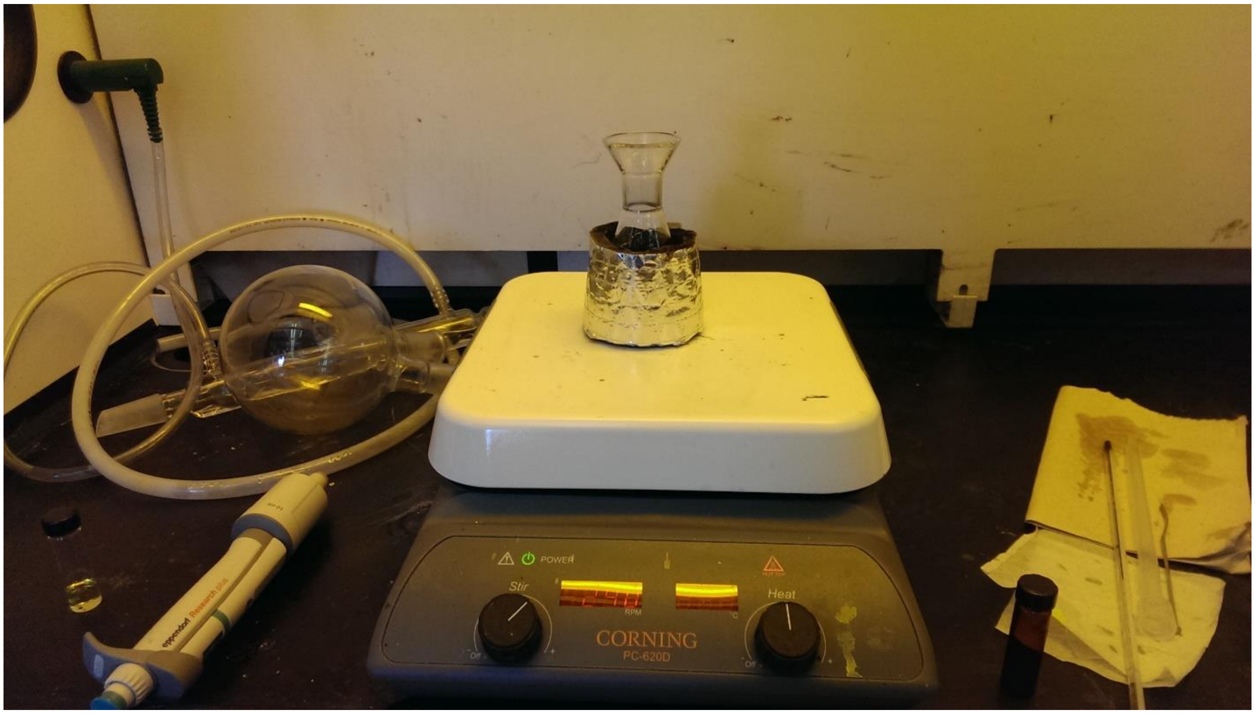

Figure 32. Polyol Synthesis Reaction Setup

When the dispersion reached the reaction temperature, a pre-weighed quantity of $AgNO_3$, 324 mg, and 4.31 mL of 0.6 mM $FeCl_3$ in EG was added all at once. This reaction mixture was heated for 1.5 hours, but it should be noted that temperature control proved challenging. The hot plate temperature setting had been set to over 200 °C to counteract the extremely slow temperature rise seen during the initial heating. Although presumed to have reached thermal steady state, the mixture was found to be boiling several minutes after the addition of $AgNO_3$ and $FeCl_3$ and the hot plate setting was immediately reduced to 160 °C to maintain the flask contents at the desired temperature for the remainder of the synthesis.

The resulting milky light brown suspension was then allowed to cool to room temperature before further separation efforts. In a typical separation, about 5 mL of the suspension was withdrawn from the flask and put into a glass sample vial. Acetone was added to this in high excess in order to precipitate the nanowires coated in insoluble PVP. Sufficient time, usually an overnight period, was given for the precipitate to settle to the bottom and side walls of the vial and for the liquid to become clear. With precipitate adhering to the glass vial, the liquid was discarded and the vial refilled with 190 proof ethanol. The vial was vigorously shaken until the precipitate was fully dispersed into the ethanol and then centrifuged at 5000 rpm for 10 min to wash any remaining ethylene glycol and free PVP. The supernatant was then discarded and the precipitate redispersed in fresh 190 proof ethanol via vigorous shaking for further characterization and experimental use.

The silver nanowire suspension in ethanol was then characterized through scanning electron microscopy, SEM, as specified below in Table IV (*Tescan Vega3 SB* Brno-Kohoutovice, Czech Republic). Samples were prepared on an aluminum stage by drop casting the suspension onto the stage and allowing to dry completely.

TABLE IV

EQUIPMENT SPECIFICATIONS

Equipment	**Manufacturer and Model Number Information**
Water Purifier	Thermo Scientific Barnstead Mega-Pure Automatic Water Distillation Apparatus
Spin Coater	Laurell WS-650MZ-23NPP/A1/AR1
Sourcemeter	Keithley Series 2400
UV-Vis Spectrometer	Perkin Elmer Lambda 950
Atomic Force Microscope	PSIA XE-100
Scanning Electron Microscope	Tescan Vega3 SB

B. PEDOT:PSS Nanocomposite Preparation and Characterization

PEDOT:PSS thin films were prepared by drop casting an aqueous dispersion of 2.1 wt. % PEDOT:PSS onto approximately 1.5 cm square slides of fluorinated tin oxide (FTO) glass and spin coating (*Laurell WS-650-MZ-23NPP/A1/AR1* North Wales, PA, USA). The FTO slides, which have a conductive side and a non-conductive side were first tested using a four point probe device connected to a source meter (*Keithley Series 2400 Sourcemeter* Cleveland, OH, USA) to identify the non-conductive side. The film was made on the non-conductive side so that the ultimately measured sample resistance would be essentially that of only the final nanocomposite. FTO slides were positioned with the non-conductive side facing up on a spin coater and held in place by vacuum. In a typical sample preparation, a few drops of PEDOT:PSS dispersion were dropped onto the center of the FTO slide until a majority of the surface was covered with no bubbles visible. The sample was then spun according to the recipe given in Table V below for the preparation of all samples. Typically, samples were prepared in batches of between three and five.

TABLE V

PEDOT:PSS SPIN COATING RECIPE

Parameter	Value
Total time	37.5 s
Maximum rotational speed setting	1500 rpm
Rotational speed acceleration	200 rpm/s

Spin coated samples were then removed from the spin coater and placed on a hot plate set to 140 °C for 20 min in order to drive off any remaining water. Sample resistances were then measured using the four point probe, one reading with the probes aligned parallel to the factory cut edge of the slide and one with the probes perpendicular to this edge. The nanocomposites were prepared by drop casting the ethanol based suspension of silver nanowires onto the surface of the PEDOT:PSS films. To create randomly oriented nanowire networks a single drop of suspension would be dropped, and the sample would be immediately placed on a hot plate set to 60 °C for 10 min to drive off the residual ethanol. The remainder of samples would be subjected to a magnetic field by positioning the glass slide between two bar magnets for 90 s and 300 s and then placed on a hot plate set to 60 °C for 10 min. The experimental setup is depicted conceptually below in Figure 33 and Figure 34.

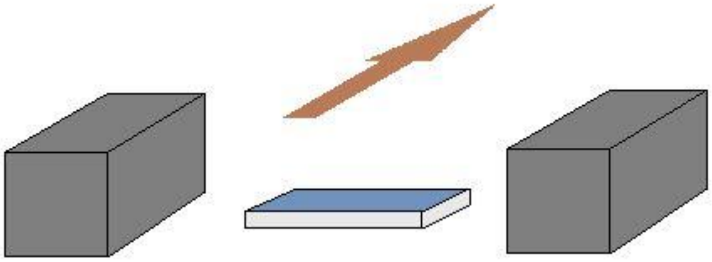

Figure 33. Three Dimensional Conceptual Diagram of Experimental Setup (Direction of Magnetic Field Shown by Arrow)

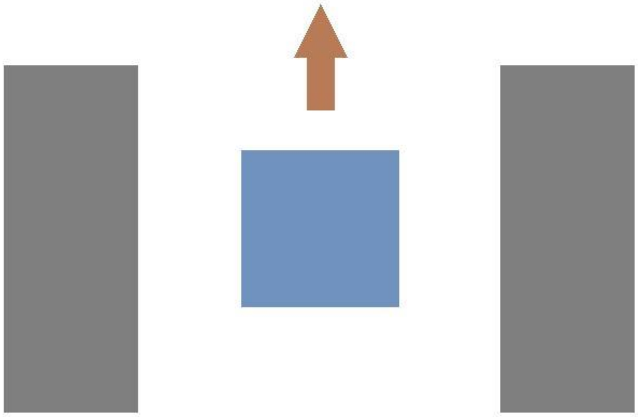

Figure 34. Conceptual Diagram of Experimental Setup (View from Top)

Samples were positioned such that magnetic field lines crossing the sample ran parallel to the factory cut edge. Parallel and transverse sample surface resistances for both groups were measured using the previously mentioned four point probe following treatment with the nanowire suspension. Parallel surface resistance measurements refer to measurements made parallel to the direction of the magnetic field lines and the expected alignment direction. Further characterization of all composite samples was then done using atomic force microscopy, AFM (*PSIA XE-100*, Santa Clara, CA, USA) and UV-Vis Spectroscopy (*Perkin Elmer Lambda 950* Waltham, MA, USA).

III. EVALUATION OF NANOCOMPOSITES: SILVER NANOWIRES ON THIN FILMS OF PEDOT:PSS

In the present thesis, we characterize the physical properties of nanocomposites consisting of PEDOT:PSS with a silver nanowire network deposited on top. In one group we evaluate the conductivity and light transmittance of samples with randomly oriented nanowire networks. In the other, we attempt to create and detect anisotropic conductivity using the magnetic field method described above.

Preceding composite preparation, silver nanowires were synthesized by the aforementioned polyol process and imaged by SEM [23]. An image is given below in Figure 35.

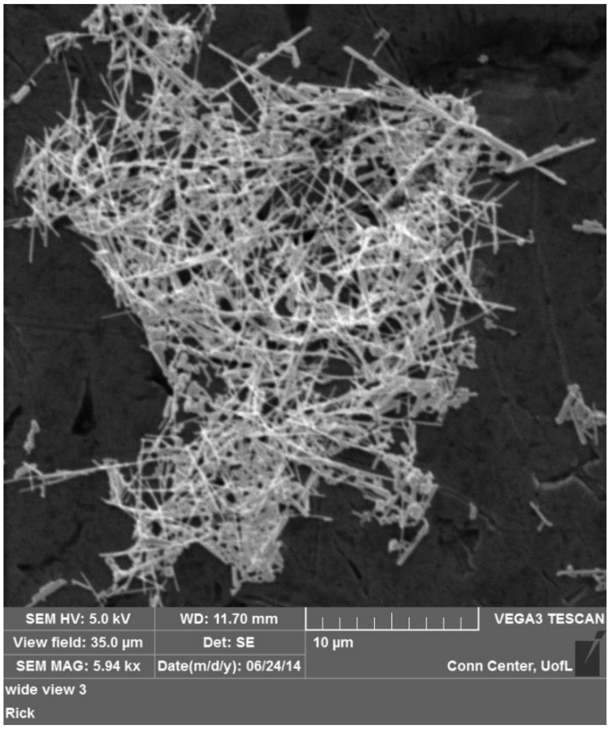

Figure 35. SEM Image of Silver Nanowires from Polyol Synthesis Route (~35 µm Square Imaging Area)

The image confirms the successful synthesis of silver nanowires. However, as noted in the previous section, the reaction temperature during synthesis did exceed that prescribed in the literature. Shorter aspect ratio nanorods and nanoparticles were also formed as significant but minor products, perhaps as a result of this temperature exceedance. Table VI below summarizes the nanowire dimensions and aspect ratio.

Table VI

DIMENSIONAL CHARACTERISTICS OF SILVER NANOWIRES

Dimension	**Mean**	**95% C.I.**
Length, µm	3.18	(2.10, 4.26)
Diameter, nm	170	(120, 220)
Aspect Ratio	20.2	(14.8, 25.6)

A. Composites with Randomly Oriented Silver Nanowire Networks

1. Data and Results

Nanocomposites were prepared without bulk alignment following the method detailed above. A photograph of a typical composite sample is shown below in Figure 36. The center and the edges of the film appear slightly darker than the intermediate region.

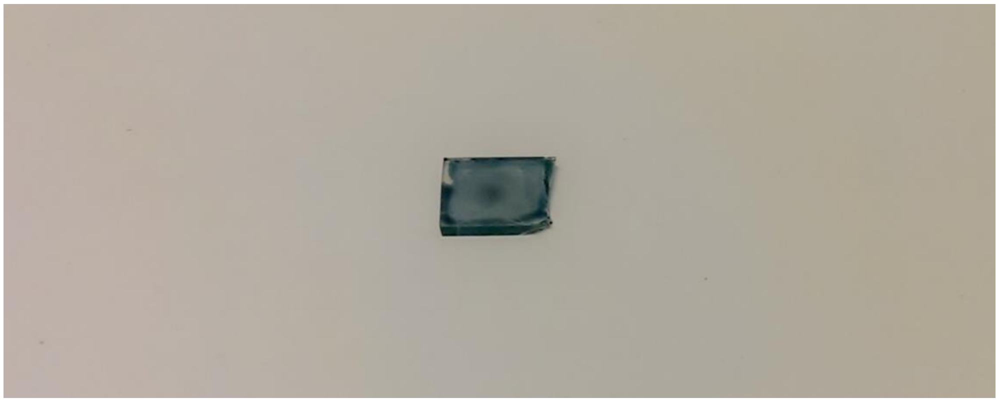

Figure 36. Photograph of a Composite Sample

As shown below in Figure 37, imaging the silver nanowire networks on the PEDOT:PSS substrate proved difficult. Although not with high clarity, some nanowires are visible. The bright portions of the image, corresponding to areas of the highest elevation, appear to be aggregates of the shorter aspect ratio nanoparticles which were not separated from the high aspect ratio nanowires.

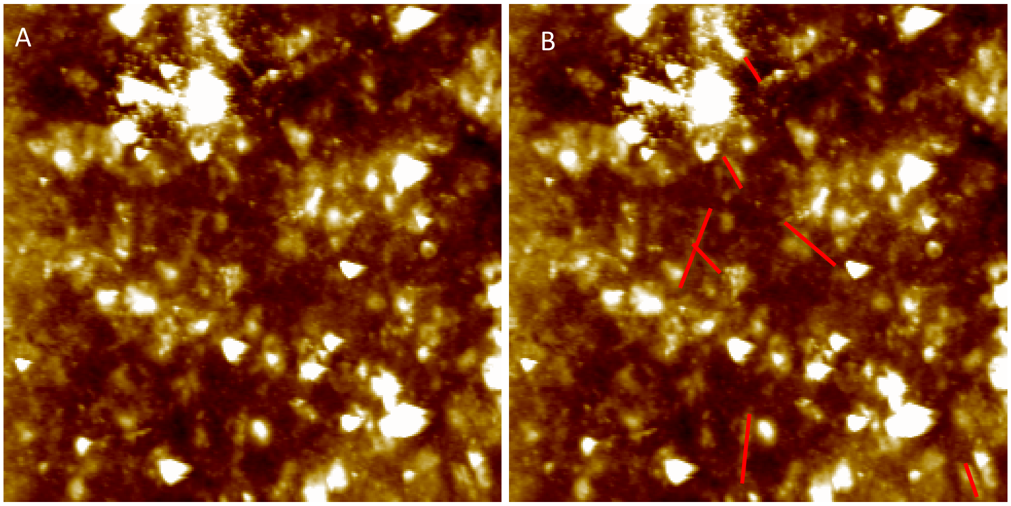

Figure 37. AFM Image of Sample **A)** Original

B) Copy with Some Nanowires Highlighted in Red (imaging area 20 µm square)

This separation into two discrete elevation ranges results from a difference in the surface area-to-volume ratio between the two classes of particles. The PVP encapsulating the nanowires, short nanorods, and spherical nanoparticles has the repeat unit structure shown below in Figure 38.

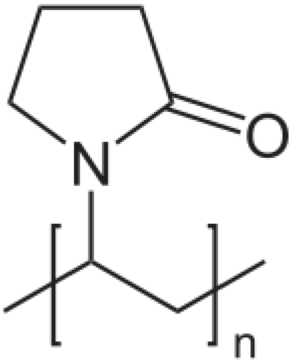

Figure 38. Repeat Unit of Polyvinylpyrrolidone, From [29]

The electron-rich oxygen and nitrogen atoms in the repeat unit exert significant intermolecular attractive forces with the polar ethanol solvent used, as well as the unregulated amount of moisture present in ambient air. Due to their very high surface area which makes for a high adhesive effect of the dipole-dipole interactions facilitated by water and ethanol, short nanorods and spherical nanoparticles tend to cluster together. Conversely, high aspect ratio nanoparticles with less surface area per volume do not experience this degree of clustering as readily, as this surface force compared to their bulk volume is significantly less. The surface area-to-volume ratio of nanoparticle *clusters*, however, is significantly lower than those of individual nanowires. Thus, one can expect that individual nanowires will more readily adhere to the surface of the electric charge-bearing PEDOT:PSS film than will short aspect ratio particle clusters, by similar reasoning in terms of surface forces. The end result is a composite with silver nanowires adhering lower to the PEDOT:PSS substrate surface, while nanoparticle clusters remain at higher surface elevations. High surface roughness results from these nanoparticle clusters, as shown below in Figure 39, which magnifies the elevation of the surface features.

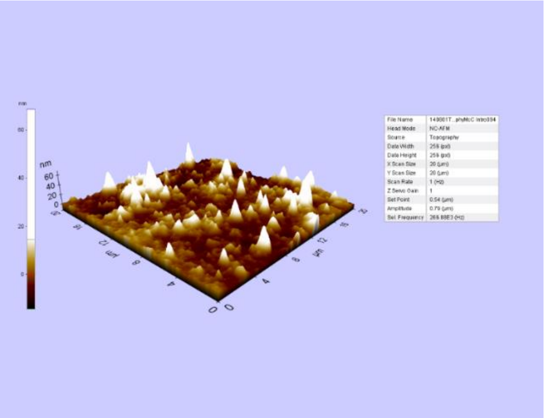

File Name	140801T...phyMcC Intro034
Head Mode	NC-AFM
Source	Topography
Data Width	256 (pxl)
Data Height	256 (pxl)
X Scan Size	20 (µm)
Y Scan Size	20 (µm)
Scan Rate	1 (Hz)
Z Servo Gain	1
Set Point	0.54 (µm)
Amplitude	0.79 (µm)
Sel. Frequency	266.88E3 (Hz)

Figure 39. Alternate View of AFM Image Showing Magnified Surface Roughness

The electrical and optical properties of the samples were also measured. It should be noted that the results presented in this work pertain to heterogeneous films, constituting a violation of the assumption of isotropic conductivity in all spatial directions. Although this may equate to some degree of offset of the reported resistances from true sheet resistances, a dimensionless parameter can be defined which essentially eliminates this error. We define the conductivity enhancement factor (EF) in terms of the following equivalent ratios:

$$E.F. = \frac{\sigma_{composite}}{\sigma_{substrate}} = \frac{R_{s,substrate}}{R_{s,composite}} \tag{12}$$

The terms $\sigma_{composite}$ and $\sigma_{substrate}$ are the conductivities of the nanocomposite and the bare PEDOT:PSS substrate film, respectively. The measured values $R_{s,composite}$ and $R_{s,substrate}$ similarly represent the sheet resistances before and after nanowire deposition. Conductivity enhancement factors are plotted versus nanowire surface concentration in Figure 40. Final sheet resistances are plotted below in Figure 41.

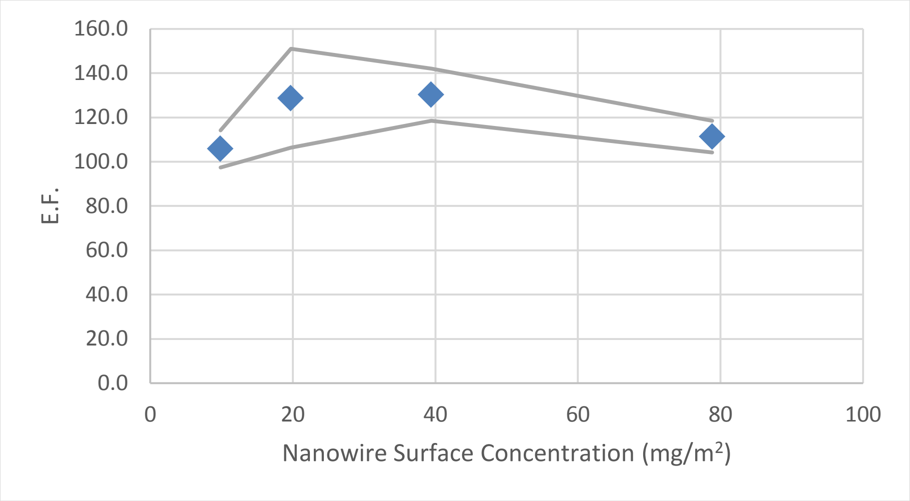

Figure 40. Plot of Conductivity Enhancement Factor vs. Surface Concentration (95% confidence boundaries shown)

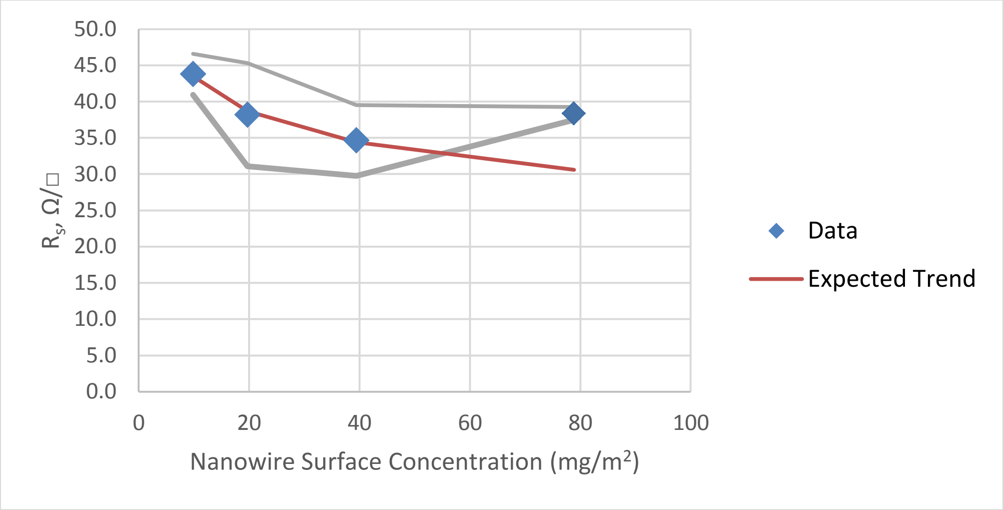

Figure 41. Plot of Final Sheet Resistance vs. Surface Concentration (95% confidence boundaries shown)

These plots convincingly show the high conductivity enhancement effect of the deposited nanowires, ranging from 110 to 135-times the initial conductivity of the PEDOT:PSS films. Discounting the large degree of error seen surrounding the second data point from the left in Figure 40, there appears to be a slight increase in the degree of enhancement going from low to medium surface concentration and a slight drop going to the highest surface concentration. Corresponding to this is an unexpected increase in R_s at the highest surface concentration. No ready explanation exists for these trends, as the degree of conductivity enhancement reported in the literature correlates positively with the surface concentration of nanowires deposited. The expected trend, as shown in Figure 41 above, is that R_s will decrease asymptotically. As the surface concentration of nanowires increases R_s should decrease by progressively smaller amounts, due to the silver nanowire more closely approaching a continuous silver layer where the addition of more silver nanowires will effect diminishing returns. Further studies using more surface concentrations both within this range and beyond it could validate the unexpected observed trend.

Figure 42 below shows the UV-Vis Transmittance Spectra for samples of different levels of nanowire surface concentration, while Figure 43 takes the average transmittance for each curve and plots it versus nanowire surface concentration.

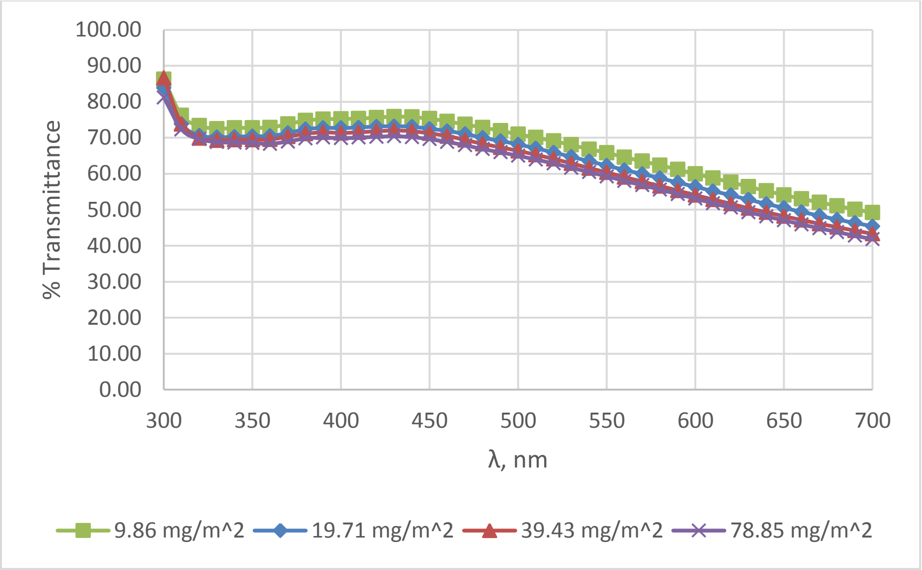

Figure 42. UV-Vis Transmittance Spectra for Samples of Various Nanowire Surface Concentrations

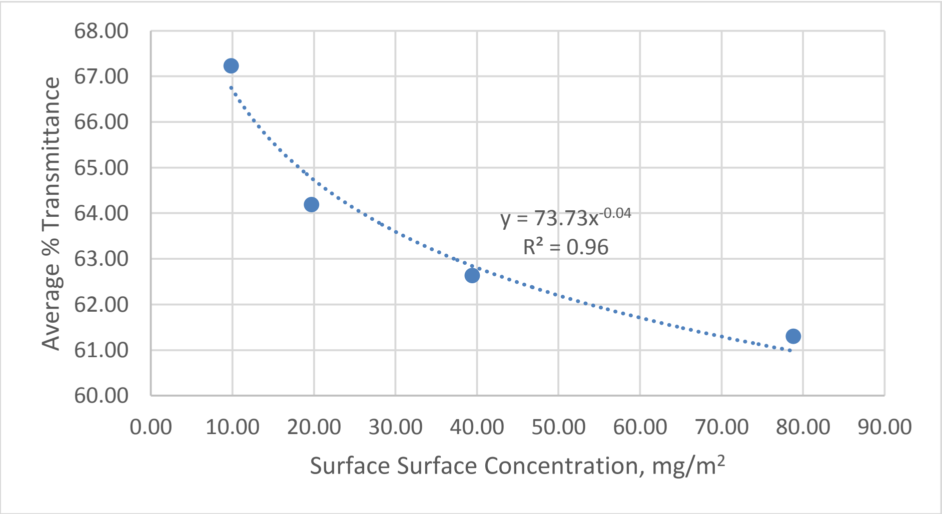

Figure 43. Plot of Average % Transmittance vs. Surface Concentration

An unmistakable trend appears in the UV-Vis data. Indeed, the percent light transmittance correlates negatively with the surface concentration as one would expect. Simple reasoning holds that the greater the quantity of nanowires present, the greater the degree of light scattering that occurs, leaving less light to transmit through the sample. It is also interesting to note that, within each UV-Vis spectrum, the percent transmittance increases with decreasing wavelength of light. The fact that the highest energy wavelengths of harvestable light have the highest transmittance attest to the viability of such a composite as either a window electrode or a counter electrode with further improvements. The power regression, while not based on first principles, offers value in modeling the expected light transmittance for a chosen nanowire surface concentration to good accuracy with $R^2 = 0.96$. Perhaps, with further work, the optical and electrical performance of silver nanowire-PEDOT:PSS composites can be more thoroughly modeled.

While the E.F. values prove to be impressively high, the combined transmittance and R_s values do not match the best values reported in the literature, which report nanowire-PEDOT:PSS composite R_s as low as 12 Ω/□ at the same average optical transmittances reported here. However, the degree of conductivity enhancement inferred from prior work is often much less than that of the present work. Indeed, the best combination of low R_s and high optical transmittance previously reported utilized PEDOT:PSS with a very high starting conductivity of ~700 S/cm, at 270 nm thickness [18]. This gives a starting R_s of around 50 Ω/□, yielding an E.F. of only about 4.4. Comparing this to the E.F. values achieved here, one sees the high value of this work despite the minor shortcoming of slightly poorer final R_s at a comparable light transmittance. One can attribute this higher-than-literature-best R_s to the quality of the silver nanowire synthesis. Indeed, the silver nanowires used by other groups are typically 5 to 10 μm in length with diameters less than 100 nm, while the nanowires synthesized here averaged 170 nm in diameter and only 3.2 μm long. The synthesis procedure can be refined so as to yield a higher percentage of higher aspect ratio nanowires, giving a higher number of nanowire interconnections for a given surface concentration and thus a lower R_s. In other words, the nanowire aspect ratio and thus junction density presents an opportunity for improvement from this work.

2. Mechanism of Conductivity Enhancement

As discussed in the introduction to this work, sheet resistance depends on two parameters, the resistivity of the film material ρ and the film thickness t by Equation (4). This of course assumes constant, anisotropic resistivity within the material. A complication thus arises considering the heterogeneous nature of the materials tested. The idea of a constant resistivity rests on the assumption of material *continuity*, wherein the constituent particle dimensions are a minute fraction of the total size of the object and the material composition is homogeneous. Although the average diameter of the nanowire inclusions (170 nm) is a significant fraction of the total film thickness (less than 400 nm) the distance of current flow along the sample width is in fact far greater than even the long dimension of the inclusions. For this reason, we accept that the assumption of continuity in composite resistivity holds along the plane of the film, even while not through its cross-section.

An increase in film thickness and thus cross-sectional area also can cause a decrease in sheet resistance. However, the 120-fold average decrease in sheet resistance observed here due to the introduction of silver nanowires is far greater than what can expected from a simple increase in film thickness. The swelling of PEDOT:PSS films with solvents such as methanol and ethanol has also been shown to cause an increase in conductivity of two orders of magnitude [1]. However, a simple study was conducted to show that the conductivity increases observed in this work did not occur as a result of this phenomenon. Figure 44 below charts the E.F. of the samples treated by drop casting nanowire suspension in ethanol against the E.F. of additional samples prepared in the same manner but with ethanol instead of nanowire suspension.

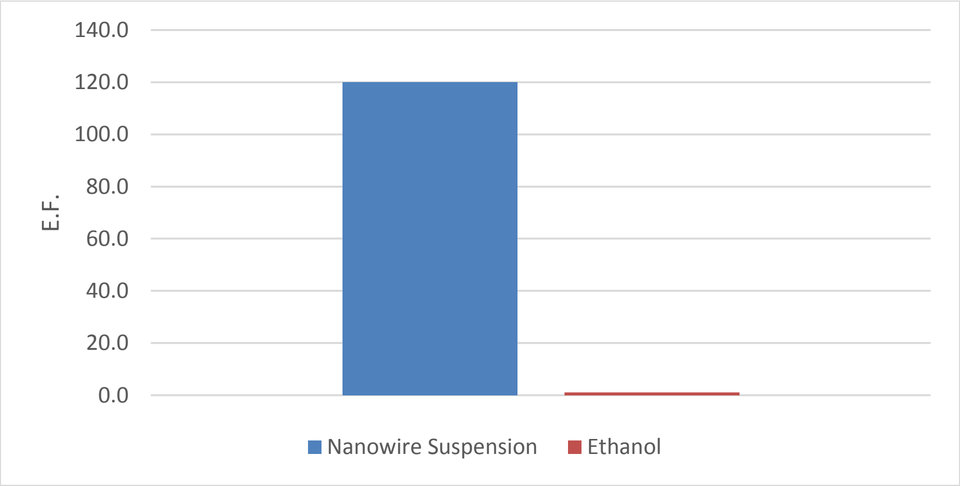

Figure 44. Conductivity Enhancement Factor Comparison

Clearly, the E.F. observed in the samples containing nanowires eclipses that of the additional samples prepared using only ethanol ($P \approx 1.3 \text{ X } 10^{-9}$). A small conductivity increase results from treatment with ethanol, but not to the degree reported by Alemu, et al. (2012). Therefore, the conductivity enhancement seen can only plausibly result from the decrease in resistivity brought by the introduction of conductive silver nanowires.

However, taking a look at initial data preceding the majority of the present work shows that the film thickness clearly has some effect on the sheet resistance. Initially, a basic study determined the effect of the maximum spin coating rotational speed on the conductivity both prior to drop-casting nanowires and following drop-casting as well as the dimensionless E.F., at constant surface concentration. Although film thickness was not directly measured, simple models of the spin-coating process corroborated by experimental measurements show that the final spin-coated polymer thickness is inversely proportional to the square root of the spin coating rotational speed, all else held constant, as shown in Equation (13) below [10].

$$t \propto \omega^{-\frac{1}{2}} \tag{13}$$

The rotational speed in units of radians per second, rad/s, is represented by ω. Thus, plotting both R_s and E.F. versus the expression on the right side of Equation (13) revealed the same graphical trends that one could expect from plotting versus measured thickness directly, as shown in Figures 45 and 46 below.

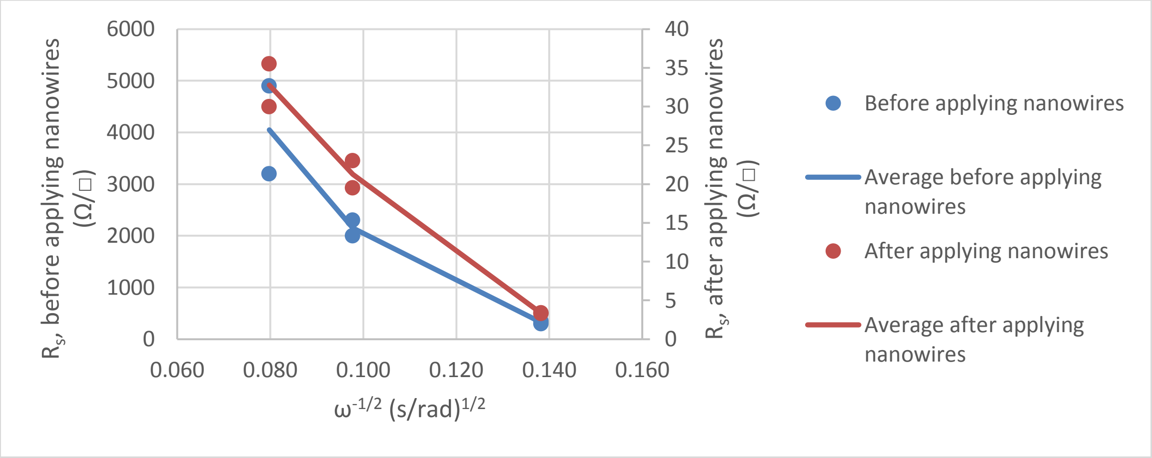

Figure 45. R_s Before and After Drop-Casting Nanowires vs. $\omega^{-1/2}$

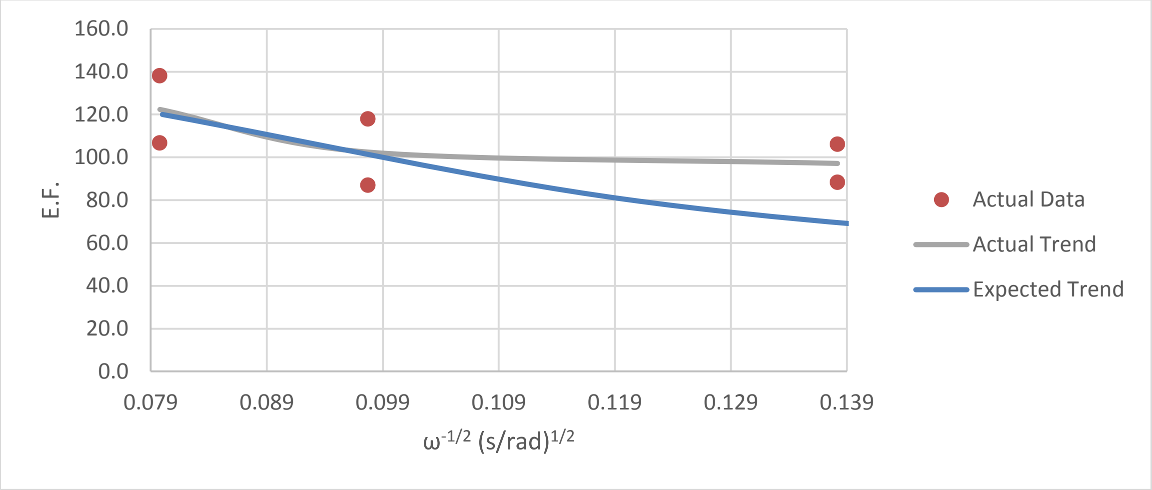

Figure 46. Conductivity Enhancement Factor vs. $\omega^{-1/2}$

One sees in Figure 45 that R_s decreases with increasing film thickness for not only the initial PEDOT:PSS substrate as expected, but also for the final composite with silver nanowires. This shows that the measurement of R_s for the final composite does depend on the final thickness to a limited extent. Indeed, while taking the measurements with the four point probe, the probes actually penetrated through the film layer, leaving small visible holes in the film. The dependence of the final R_s measurement on thickness suggests that a certain fraction of current flows through the PEDOT:PSS layer below the silver nanowire layer. If all current flowed through the top silver nanowire layer, a constant final R_s would be expected. However, the simple fact that R_s measured after drop-casting is much lower than that measured before drop-casting confirms that the deposition of nanowires does in fact have a large effect on the film R_s, regardless of the thickness dependence seen.

Examining Figure 46, one sees the trend of E.F. with respect to film thickness. Based on the penetration of the probes which send electrical current, one expects that for a thicker starting substrate film, a larger fraction of current will travel through the substrate film itself, as illustrated in Figure 47 below.

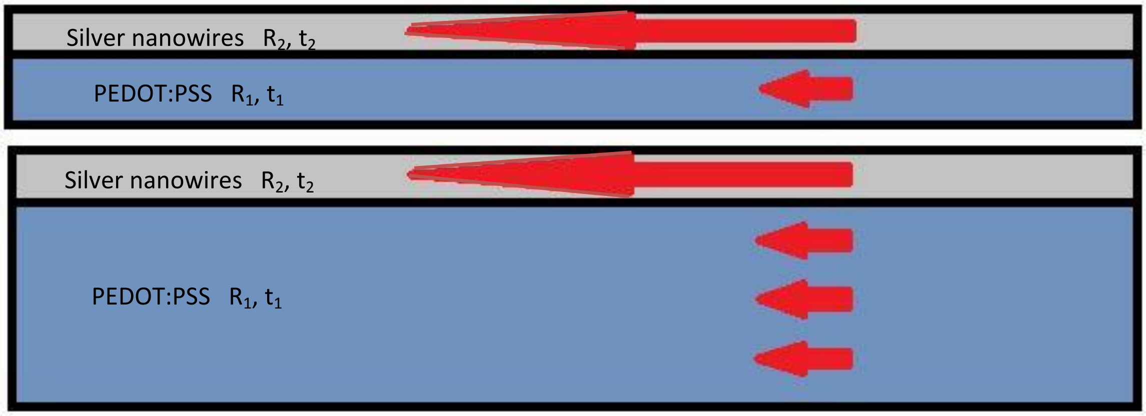

Figure 47. Representation of Relative Current Distribution through Film Cross-Section for Both Thin (top) and Thick (bottom) PEDOT:PSS Layers, Magnitude of Current Represented by Length of Arrows

One can see evidence of this in the degree of E.F. versus thickness in Figure 46. At lower thickness a higher E.F. is seen due to a higher fraction of current flowing through the more conductive silver nanowire layer. As thickness increases, E.F. decreases because a higher fraction of current flows through the PEDOT:PSS substrate itself. This follows from the predictable decrease in R_s of the substrate accompanying increasing thickness. However, this downward trend of E.F. vs. thickness asymptotically approaches a minimum limit. One can anticipate this trend by modeling the composite resistance in terms of the resistances of the individual layers (as designated above in Figure 47) in parallel:

$$E.F. = \frac{R_1}{R_{composite}} = \frac{R_1}{\left(\frac{1}{R_1} + \frac{1}{R_2}\right)^{-1}} = \frac{R_1}{R_2} + 1 = \frac{\rho_1}{R_2 t_1} + 1 = \frac{C}{\omega^{-\frac{1}{2}}} + 1 \qquad (14)$$

Essentially, the only variable is ω. By fitting the predicted value of E.F. to match the actual measured value at the lowest thickness (highest ω) by adjusting the constant C, one generates the expected trend curve shown above in Figure 46. The expected E.F. fits the actual data well through the low and medium thickness data points, but deviates from the actual at the highest thickness, potentially because of the penetration of the voltage-measuring probes completely through the film. The skewing effect that this penetration of the probes has on the final measurement should naturally be larger for a larger film thickness. For this reason, it was assumed that the model is more accurate at lower thicknesses and thus the model was forced to fit the lowest as opposed to the highest thickness data point.

In sum, by looking at constant thickness data, the enhancement of conductivity observed clearly results mainly by the introduction of a conductive silver nanowire layer. However, by virtue of the measurement, wherein the probes actually penetrated the film, the current flowed through the PEDOT:PSS substrate itself and not only the silver nanowire layer. By varying PEDOT:PSS thickness and holding the surface concentration constant, the asymptotically decreasing E.F. versus thickness was seen and compared to a model based on parallel resistances.

B. Evaluation of Magnetic Alignment Technique

In the present thesis, we report on the feasibility of a technique to align silver nanowires on a PEDOT:PSS film using a magnetic field. While van Rhee, et al. (2013) has reported on the magnetic susceptibility of low aspect ratio *gold nanorods* to a significantly greater degree than bulk gold, nowhere in the literature as far as we are aware has the same concept been applied to higher aspect ratio nanowires of *silver*, an element with electron orbital characteristics similar to that of gold. Building upon the finding that the degree of anisotropic magnetic susceptibility correlates positively with nanoparticle aspect ratio, the use of high aspect ratio silver nanowires showed promise. This effort searched for anisotropy in conductivity. Results for the ratio of parallel resistance to transverse resistance as measured using a four point probe in the manner outlined in the previous section are summarized graphically below in Figure 48.

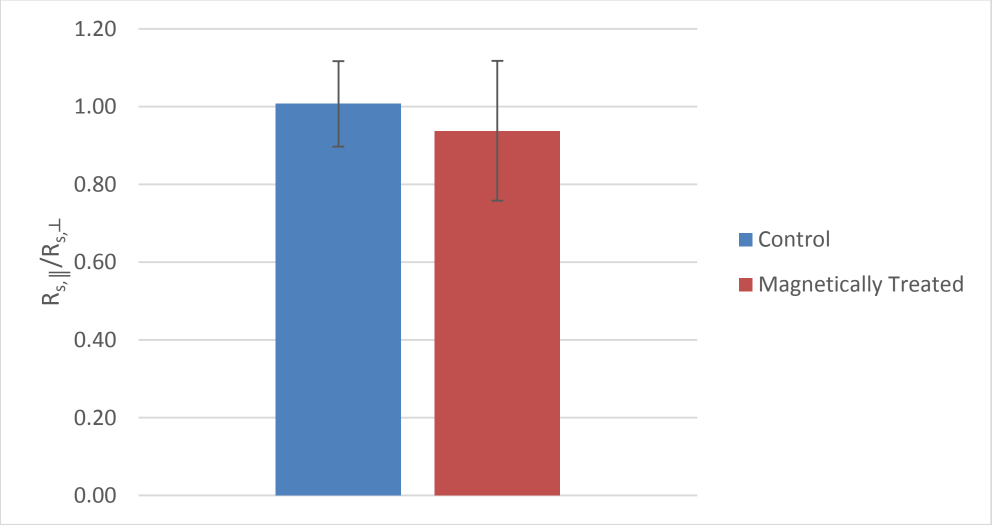

Figure 48. Resistance Ratio for Control and Experimental Samples (error bars shown, α=0.05)

The results show a slight reduction in the resistance ratio for the samples subjected to the magnetic field treatment but with significant calculated error rendering the results inconclusive under these conditions. One can attribute the variability observed to a number of uncontrolled factors. An uneven distribution of silver nanowires over the surface of the PEDOT:PSS film could easily mask any true magnetic alignment as measured by surface resistance. Furthermore, the surface irregularities of the PEDOT:PSS surface could have even prevented the alignment process by inhibiting rotation of the nanowires. Indeed, the AFM images highlighted above show silver nanoparticle clusters protruding to heights up to 50 nm. This problem could be overcome by drop casting the nanowire suspension onto the glass substrate first, then treating it with the magnetic field in an ethanol saturated atmosphere to slow evaporation of ethanol from the sample surface and allow sufficient mobility for nanowire rotation. Subsequently, PEDOT:PSS can be deposited onto this layer. However, this option was not pursued because the original intent was to image nanowires on the top surface of the film.

Yet another possible explanation for the lack of anisotropic conductivity seen lies in the dynamics at play in the evaporation of ethanol from the sample surface. While subjected to the magnetic field, the samples remained at room temperature. Unlike the samples discussed in the preceding sections, these samples experienced initially a significantly slower ethanol evaporation rate. Under these slower drying conditions, the droplet of liquid would more gradually shrink inward, and could have induced a degree of alignment not accounted for. The inward migration of the three phase interface, the boundary between the solid substrate, the liquid ethanol-based suspension, and ambient air, could have imposed its own driving force with two possible alignment schemes illustrated conceptually below in Figure 49. Either circumferential alignment can occur as the nanowires align along the edge of the moving interface by intermolecular dipole-dipole interactions with the ethanol, or radial alignment can occur as the nanowires align with the direction of migration of this interface through a drag force.

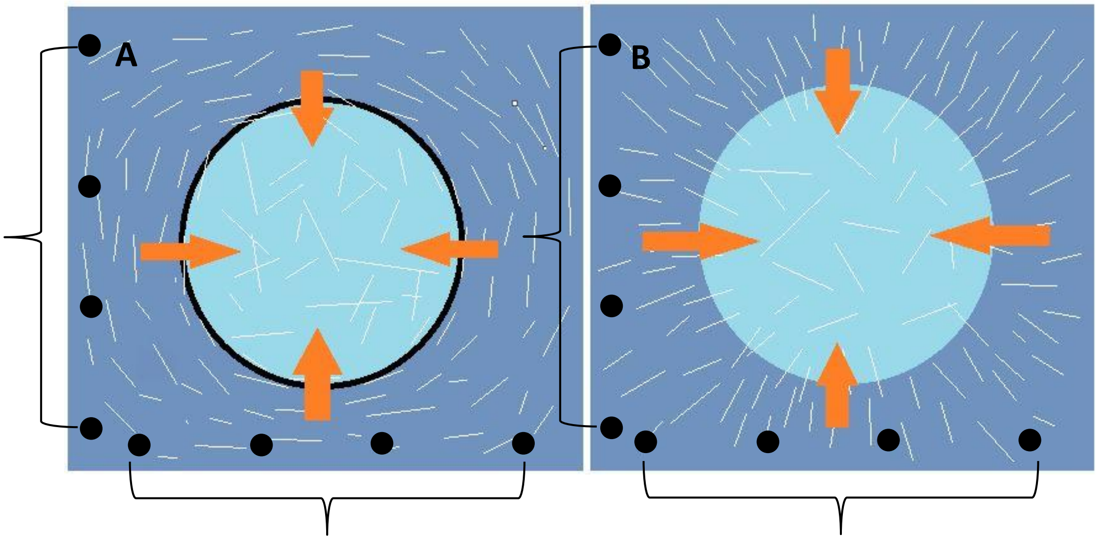

Figure 49. Possible Alignment Schemes A) Circumferential (interface of alignment in bold) B) Radial, Direction of Interface Migration Shown By Arrows in Both Cases

That this drying step occurred at room temperature also makes for a lower degree of random thermal forces relative to this potential alignment force, making either of these alignment mechanisms potentially more dominant than the effect of the magnetic field. Realistically, the radial or circumferential alignment effects cannot be anticipated to occur in the center region of the sample as the moving interface shrinks inward in the final phase of evaporation, as the driving force for alignment becomes weaker than other forces at play. For this reason, the difference in mean resistance ratios seen in Figure 48 can be attributed to the magnetic alignment occurring in the sample center, while the magnitude of variability seen can be attributed to the fact that probe measurements were taken near the sample edge, away from this zone of potentially aligned nanowires. Figure 50 below shows that this positioning of the probes was necessary due to a set of two probes (top two black dots) which needed to be pressed to the surface in order to generate a measurement using the four main probes (bottom four black dots). Figure 51 below shows the photograph of a sample with overlaid dots at the approximate contact points of the four measurement probes.

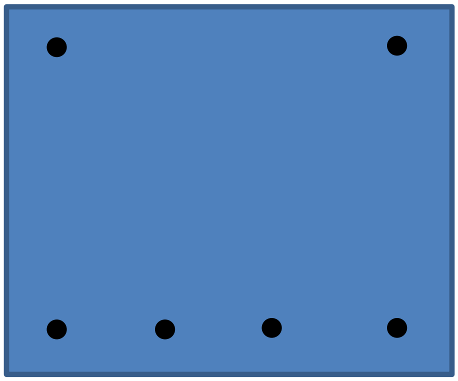

Figure 50. Layout of All Contact Points for Four Point Probe Measurement on Sample Surface

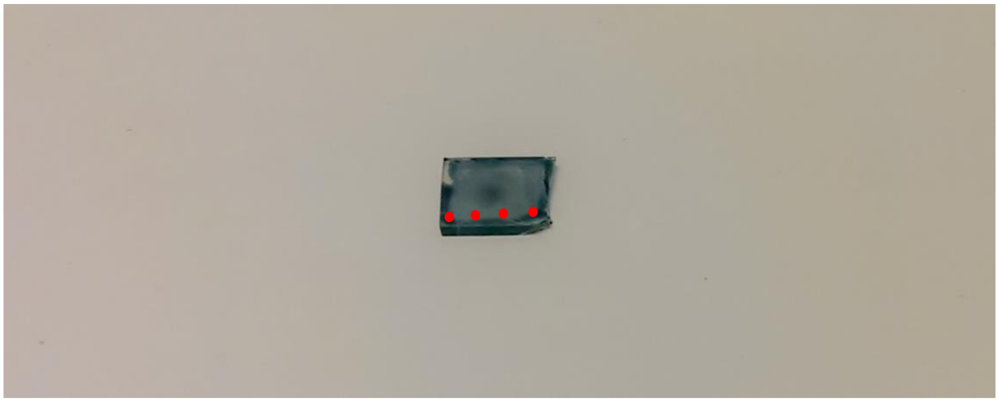

Figure 51. Photograph of Composite Sample with Overlaid Dots at Approximate Probe Contact Points

IV. CONCLUSIONS

Silver nanowires were synthesized with lengths of 3.18 ± 1.08 μm and diameters of 170 nm ± 50 nm, giving an average aspect ratio of 20.20 ± 5.43 ($\alpha = 0.05$). Composites of PEDOT:PSS with a randomly oriented silver nanowire network deposited by drop casting possessed average sheet resistances of 36.7 Ω/□ and an average increase in conductivity from the base PEDOT:PSS film of 120-fold. In accordance with the literature, a negative correlation between UV-Vis light transmittance and nanowire surface concentration within the range of surface concentrations tested was detected and fit to a power regression ($R^2 = 0.96$). However, contrary to the literature, no steady negative correlation was detected between sample sheet resistance and nanowire surface concentration in this range, 9.9 mg/m^2 to 79 mg/m^2. Sheet resistance and conductivity enhancement factor data for varying PEDOT:PSS thicknesses and constant nanowire surface concentration showed an asymptotically decreasing enhancement factor versus film thickness. The magnetic nanowire alignment technique yielded slightly anisotropic conductivities, but with high statistical error.

V. RECOMMENDATIONS FOR FUTURE WORK

The course of the present thesis revealed opportunities for improvement in the experimental design. The synthesis of silver nanowires must be improved, specifically with tighter temperature control. Additionally, for an even distribution of nanowires in a randomly oriented network to be achievable, nanowire suspensions should be used as quickly as possible in order to prevent agglomeration. A further suggestion would be to employ sonication just prior to drop casting as a further mitigating measure. Following these suggestions, an even distribution of high aspect ratio nanowires is more likely, with the main intent of further decreasing sheet resistance by increasing the number of junctions per unit area across the entire film surface.

The fact remains that the silver nanowires used in these studies had a layer of high molecular weight PVP coating them. If a method could be developed to remove this coating, then the nanowire junction resistance could be reduced, significantly improving film conductivity. However, considering that the polyol method for nanowire synthesis already involves several steps and demands tighter temperature control, room temperature syntheses may also be favorable over this method.

The relatively weak anisotropy in conductivity of the samples subjected to magnetic treatment in this work could have resulted from a variety of causes. One, as addressed above, may have been non-uniformity in deposition on the surface. Any tendencies for unpredictable agglomeration on the surface could easily mask anisotropy in conductivity regardless of the effectiveness of the magnetic treatment. Furthermore, the drag force from the evaporation of ethanol from the drop-cast suspension may also have inhibited the alignment of the nanowires with the magnetic field over a majority of the sample surface. A moderate or rapid evaporation rate can lead to unwanted components of motion, upsetting the process of alignment. With a very slow, controlled evaporation rate, these undesired components of motion can be eliminated, leaving only the driving force of the magnetic field to be truly studied. A challenge here would exist in preventing agglomeration during this slow drying step, and ensuring that the interactions between the surface of the nanowires and the substrate is great enough to prevent disturbance by the evaporating solvent as well as any surface agglomeration.

Another approach to isolate the magnetic alignment effect would be to disperse the nanowires directly into the PEDOT:PSS dispersion, conduct the alignment, and subsequently evaporate the water to leave a composite film with aligned nanowires. Additional PEDOT:PSS can be deposited on top of this electrode layer to provide the hole transport layer for incorporation into a DSSC device.

Yet another possibility for future endeavors would be to adapt the work of Jiu, et al. (2012) and employ high intensity pulsed light to essentially fuse together nanowires, and thus decrease junction resistance. A challenge here would be to tune the exposure time and intensity of light such that only the nanowires experience heating and the substrate remain undamaged.

Finally, the issue with penetration of the resistance measurement probes through the films, though it ultimately yielded insight into the mechanism of conductivity enhancement, poses another opportunity for refinement. If probes with tips made of a softer material such as beryllium and with a broader radius of curvature could be used, the confinement of electrical current to the conductive silver nanowire layer can be confirmed. This differential conductivity is desirable for a combination hole-transport layer and counter electrode material for use in organic solar cells.

REFERENCES CITED

1. Alemu, D., et al. 2012. Highly conductive PEDOT:PSS electrode by simple film treatment with methanol for ITO-free polymer solar cells. *Energy & Environmental Science* 5. 11: p. 9662-9671.

2. Cao, Y., et al. 2006. A technique for controlling the alignment of silver nanowires with an electric field. *Nanotechnology* 17. 9: p. 2378-2380.

3. Chen, C. C., et al. 2012. Visibly Transparent Polymer Solar Cells by Solution Processing. *ACS Nano* 6. 8: p. 7185-7190.

4. Chung, I., et al. 2012. All-solid-state dye-sensitized solar cells with high efficiency. *Nature* 485. 7399: p. 486-494.

5. Correa-Duarte, M. A., et al. 2005. Aligning au nanorods by using carbon nanotubes as templates. *Angewandte Chemie-International Edition* 44. 28: p. 4375-4378

6. Hagfeldt, A., et al. 2010. Dye-sensitized solar cells. *Chemical Reviews* 110. 11: p. 6595-6663.

7. Hangarter, C. M., et al. 2005. Magnetic alignment of nanowires. *Chemistry of Materials* 17. 6: p. 1320-1324.

8. Hangarter, C. M., et al. 2007. Hierarchical magnetic assembly of nanowires. *Nanotechnology* 18. 20: p. 7.

9. Hu, L. B., et al. 2010. Scalable Coating and Properties of Transparent, Flexible, Silver Nanowire Electrodes. *ACS Nano* 4. 5: p. 2955-2963.

10. Jaeger, R. C. 2002. *Introduction to Microelectronic Fabrication, Second Edition.* Upper Saddle River: Prentice Hall.

11. Jana, N. R., Gearheart, L., and Murphy, C. J. 2001. Wet chemical synthesis of silver nanorods and nanowires of controllable aspect ratio. *Chemical Communications*. 7: p. 617-618.

12. Jiu., J., et al. 2012. Strongly adhesive and flexible transparent silver nanowire conductive films fabricated with a high-intensity pulsed light technique. *Journal of Materials Chemistry* 22. 44: p. 23561-23567.

13. Kanagawa, M., et al. 2001. Correction factor for four-probe resistivity measurements on resistive sheets with parallel electrodes. *Electronics and Communications in Japan Part I- Electronics* 84. 9: p. 36-45.

14. Korte, K. E., Skrabalak, S. E., and Xia, Y. N. 2008. Rapid synthesis of silver nanowires through a CuCl- or CuCl2- mediated polyol process. *Journal of Materials Chemistry* 18. 4: p. 437-441.

15. Langley, D. P., et al. 2014. Silver nanowire networks: Physical properties and potential integration in solar cells. *Solar Energy Materials and Solar Cells* 125. p. 318-324.

16. Law, M., et al. 2005. Nanowire dye-sensitized solar cells. *Nature Materials* 4. 6: p. 455-459.

17. Murphy, C. J., et al. 2005. Anisotropic metal nanoparticles: Synthesis, assembly, and optical applications. *Journal of Physical Chemistry B* 109. 29: p. 13857-13870.

18. Noh, Y. J., et al. 2014. Cost-effective ITO free organic solar cells with silver nanowire-PEDOT:PSS composite electrodes via a one-step spray depostion method. *Solar Energy Materials and Solar Cells* 120. p. 226-230.

19. Oregan, B. and Grätzel, M. 1991. A low cost, high efficiency solar-cell based on dye-sensitized colloidal TiO2 films. *Nature* 353. 6346: p. 737-740.

20. Schroder, D. K. 2006. *Semiconductor Material and Device Characterization, Third Edition*. New York City: Wiley-IEEE Press.

21. Shi, H. Y., et al. 2010. Ordering of Disordered Nanowires: Spontaneous Formation of Highly Aligned, Ultralong Ag Nanowire Films at Oil-Water-Air Interface. *Advanced Functional Materials* 20. 6: p. 958-964.

22. Sommeling, P. M., et al. 2004. Long-term stability of dye-sensitized solar cells. *Journal of Photochemistry and Photobiology and Chemistry* 164. 1-3: p. 137-144.

23. Sun, Y. G. and Xia, Y. N. 2002. Large-scale synthesis of uniform silver nanowires through a soft, self-seeding, polyol process. *Advanced Materials* 14. 11: p. 833-837.

24. Tao, A., et al. 2003. Langmuir-Blodgett silver nanowire monolayers for molecular sensing surface-enhanced Raman spectroscopy. *Nano Letters* 3. 9: 1229-1233.

25. van de Lagemaat and Frank, A. J. 2001. Nonthermalized electron transport in dye-sensitized nanocrystalline TiO2 films: Transient photocurrent and random-walk modeling studies. *Journal of Physical Chemistry B* 105. 45: p. 11194-11205.

26. van Rhee, P. G. , et al. 2013. Giant Magnetic Susceptibility of Gold Nanorods Detected by Magnetic Alignment. *Physical Review Letters* 111. 12: p. 5.

27. Walter, E. C., et al. 2002. Noble and coinage metal nanowires by electrochemical step edge decoration. *Journal of Physical Chemistry B* 106. 44: p. 11407-11411.

28. Wei, G., et al. 2005. One-step synthesis of silver nanoparticles, nanorods, and nanowires on the surface of a DNA network. *Journal of Physical Chemistry B* 109. 18: p. 8738-8743.

29. Wikipedia Contributors. *Polyvinylpyrrolidone*. Wikipedia, the Free Encyoclopedia [cited 2014 November 1]; Available from: http://en.wikipedia.org/wiki/Polyvinylpyrrolidone

30. Wiley, B., Sun, Y. G., and Xia, Y.N. 2005. Polyol synthesis of silver nanostructures: Control of product morphology with Fe(II) or Fe(III) species. *Langmuir* 21. 18: p. 8077-8080.

31. Xiong, Y. J., et al. 2003. Growth of well-aligned gamma-MnO2 monocrystalline nanowires through a coordination-polymer-precursos route. *Chemistry-A European Journal* 9.7: p. 1645-1651.

32. Zeng, X. Y., et al. 2010. A New Transparent Conductor: Silver Nanowire Film Buried at the Surface of a Transparent Polymer. *Advanced Materials* 22. 40: p. 4484.

APPENDIX

TABLE VII

SHEET RESISTANCE DATA FOR NON-ALIGNED SAMPLES

Sample	**Nanowire Surface Concentration (mg/m^2)**	**R_s, Ω/□ (before drop casting)**	**R_s, Ω/□ (after drop casting)**
1	78.85	4300	38.5
2	78.85	3800	37.0
3	78.85	4550	38.5
4	78.85	4200	39.1
5	78.85	4520	38.7
6	39.43	4700	37.4
7	39.43	4800	32.5
8	39.43	3600	28.1
9	39.43	4700	36.1
10	39.43	4670	39.1
11	19.71	4800	39.5
12	19.71	4800	37.6
13	19.71	4740	33.1
14	19.71	4810	48.3
15	19.71	4900	32.4
16	9.86	4400	44.0
17	9.86	4700	39.9
18	9.86	4770	45.9
19	9.86	4630	43.0
20	9.86	4590	46.1

TABLE VIII

SHEET RESISTANCE DATA FOR MAGNETIC ALIGNMENT

Sample	**Magnet Exposure Time (s)**	**$R_{s,\parallel}$ before drop casting (Ω/□)**	**$R_{s,\perp}$ before drop casting (Ω/□)**	**R_s Ratio**	**$R_{s,\parallel}$ after drop casting (Ω/□)**	**$R_{s,\perp}$ after drop casting (Ω/□)**	**R_s Ratio**
1	0	4800	4600	1.04	33.9	35.8	0.95
2	0	3700	4500	0.82	36.4	34.4	1.06
3	0	4000	5400	0.74	31	28.4	1.09
4	0	4300	4500	0.96	35.1	37.7	0.93
5	120	4500	3900	1.15	29.5	29.0	1.02
6	120	3200	3700	0.86	24.2	27.0	0.90
7	120	3900	4000	0.98	26.8	24.6	1.09
8	120	3700	3300	1.12	27.4	34.5	0.79

TABLE IX

DATA FOR TREATMENT OF PEDOT:PSS FILMS WITH 190 PROOF ETHANOL

Sample	**R_s, Ω/□ (before drop casting)**	**R_s, Ω/□ (after drop casting)**	**E.F.**
1	4930	3890	1.27
2	4810	4220	1.14
3	4850	4200	1.15
4	4670	4480	1.04
5	4900	4200	1.17

VITA

Richard Korte was born June 21, 1991 aboard the naval aircraft carrier U.S.S. Peleliu near the Philippines in the wake of the eruption of Mt. Pinatubo. For most of his life he has resided in Bowling Green, KY, where he graduated from Bowling Green High School in May 2009.

Richard attended the University of Louisville beginning in 2009. During the Spring Semester of 2011, Fall Semester of 2011, and Summer Semester of 2012 he worked as an engineering co-op at SABIC Innovative Plastics in Mount Vernon, IN. During the Fall Semester of 2013 and Spring Semester of 2014, he worked as a mathematics tutor at the University of Louisville Resources for Academic Achievement (REACH). He earned his Bachelor of Science degree in Chemical Engineering in May 2013 and will graduate with a Master of Engineering in Chemical Engineering in December 2014. Richard plans to continue to work in the chemical industry following the completion of his Master of Engineering degree.